

# Disruptions, disruptivity and safer operating windows in the high- $\beta$ spherical torus NSTX

S.P. Gerhardt<sup>1</sup>, R.E. Bell<sup>1</sup>, A. Diallo<sup>1</sup>, D. Gates<sup>1</sup>, B.P. LeBlanc<sup>1</sup>,  
J.E. Menard<sup>1</sup>, D. Mueller<sup>1</sup>, S.A. Sabbagh<sup>2</sup>, V. Soukhanovskii<sup>3</sup>,  
K. Tritz<sup>4</sup> and H. Yuh<sup>5</sup>

<sup>1</sup> Princeton Plasma Physics Laboratory, Princeton NJ 08543, USA

<sup>2</sup> Department of Applied Physics, Columbia University, New York, NY 10027, USA

<sup>3</sup> Lawrence Livermore National Laboratory, Livermore, CA 94551, USA

<sup>4</sup> The Johns Hopkins University, Baltimore, MD 21218, USA

<sup>5</sup> Nova Photonics, Princeton NJ 08540, USA

Received 21 September 2012, accepted for publication 1 March 2013

Published 8 April 2013

Online at [stacks.iop.org/NF/53/043020](http://stacks.iop.org/NF/53/043020)

## Abstract

This paper discusses disruption rates, disruption causes and disruptivity statistics in the high- $\beta_N$  National Spherical Torus Experiment (NSTX) (Ono *et al* 2000 *Nucl. Fusion* **40** 557). While the overall disruption rate is rather high, configurations with high  $\beta_N$ , moderate  $q^*$ , strong boundary shaping, sufficient rotation and broad pressure and current profiles are found to have the lowest disruptivity; active  $n = 1$  control further reduces the disruptivity. The disruptivity increases rapidly for  $q^* < 2.7$ , which is substantially above the ideal MHD current limit. Under quiescent conditions,  $q_{\min} > 1.25$  is generally acceptable for avoiding the onset of core rotating  $n = 1$  kink/tearing modes; when EPM and ELM disturbances are present, the required  $q_{\min}$  for avoiding those modes is raised to  $\sim 1.5$ . The current ramp and early flat-top phase of the discharges are prone to  $n = 1$  core rotating modes locking to the wall, leading to a disruption. Small changes to the discharge fuelling during this phase can often mitigate the rotation damping associated with these modes and eliminate the disruption. The largest stored-energy disruptions are those that occur at high current when a plasma current ramp-down is initiated incorrectly.

(Some figures may appear in colour only in the online journal)

## 1. Introduction

Tokamaks and ST plasmas are prone to events known as disruptions, where a catastrophic loss of confinement leads to the rapid quench of the plasma current. The loss of energy confinement can lead to severe thermal loads on the plasma-facing components (PFCs) [1–8], while the electromagnetic loads from the ‘current quench’ [9–14] can lead to excessive mechanical loads [15]. The current quench can also lead to the generation of runaway electrons [6, 7, 16–21], which can result in vessel and PFC damage [33]. Finally, if the control of the plasma vertical position [23–27] is lost, the plasma can drift up or down and come in contact with the vessel and PFCs; the ‘halo currents’ [28–34] that are shared between those components and the plasma can lead to large forces on those components [15].

The disruptive stability boundaries have traditionally been considered in terms of certain global parameters [35]. The limit on the plasma pressure is typically quoted in terms of the

normalized  $\beta$ , defined as  $\beta_N = a B_T \beta_T / I_P$  [36]. In the absence of a conducting wall, the value of  $\beta_N$  at which instabilities occur depends on the aspect ratio [37, 38], boundary shape [39, 40] and the shape of the current and pressure profiles [37, 39, 41]. When a conducting wall is present, image currents in the wall can provide a stabilizing effect, and the  $\beta_N$  limit can be higher. However, a new branch of the high- $\beta$  kink instability can become unstable due the tendency of these currents to resistively dissipate. This instability, known as the resistive wall mode (RWM) [42, 43], has been observed in both conventional aspect-ratio tokamaks [44, 45] and in STs [46–50]. It can be stabilized by the presence of rotation and dissipation [42, 43]. Alternatively, because the RWM growth rate is the comparatively slow  $L/R$  time of the relevant eddy current path in the conducting wall, direct feedback control using non-axisymmetric coils can be used [51, 52].

The plasma current limit is typically written in terms of the edge safety factor  $q$ , often quoted at the flux surface containing 95% of the poloidal flux and denoted  $q_{95}$ , or as

the cylindrical safety factor  $q^* = (\varepsilon\pi a B_T / \mu_0 I_P)(1 + \kappa^2)$ . Ideal MHD calculations have shown  $q^*$  is indeed a better aspect-ratio independent measure of the current limit [53], with values less than  $\sim 1.3$  leading to ideal instability at any value of  $\beta_N$ . Early experiments in JET showed a clear disruptive boundary at  $q_{\text{edge}} = 2$  [54]; the lowest achievable  $q_{95}$  in PBX was  $\sim 2.2$  [55]. More recent work in JET has shown a clear increase in disruptivity for  $q_{95} < 2.5$  [56]. In order to avoid these disruptions, ITER will operate at  $q_{95} \approx 3$ , corresponding to  $q^* \approx 2.5$  (using  $I_P = 15$  MA,  $B_T = 5.3$  T,  $R_0 = 6.2$  m,  $a = 2.0$  m and  $\kappa = 1.85$  [57]). For the ST, [53] showed initial data that the low- $q$  boundary may indeed occur at  $q^*$  of  $\sim 1.3$ .

An additional disruptive stability limit is related to the plasma density [58–62]. This is normally captured by the Greenwald fraction [61],  $f_{\text{GW}} = \bar{n}_e / n_{\text{GW}}$ , where  $\bar{n}_e$  is the line-averaged density and  $n_{\text{GW}} = I_P / \pi a^2$ , with  $I_P$  in MA and  $n_{\text{GW}}$  in units of  $10^{20} \text{ m}^{-3}$ . In H-mode [63], exceeding the density limit typically results in a back transition to L-mode. In L-mode, exceeding the density limit typically results in a disruption. This disruption is often associated with the cooling of the plasma edge and an increase in radiation [54], and there is evidence that formation of magnetic islands may play an important role in this process [62, 64–66].

Finally, the formation of magnetic islands has been observed to limit the plasma  $\beta$ , even at densities significantly lower than the Greenwald limit. The most commonly considered form of such instabilities are the neoclassical tearing modes (NTMs) [67–72], which occur in plasmas with a reasonably high bootstrap current fraction. These modes arise from the flattening of the temperature profile within a magnetic island: the resulting reduction in bootstrap current leads to a negative current perturbation, which reinforces the growth of the island for conventional positive tokamak magnetic shear. While  $n \geq 2$  NTMs generally manifest themselves as a loss of confinement,  $n = 1$  NTMs can slow the plasma rotation and lock to the wall, often leading to disruption. Note that while the majority of NTM research has been conducted in conventional aspect-ratio tokamaks, they have also been observed in the spherical torii NSTX [73, 74] and MAST [75, 76].

An important aspect of disruption avoidance is active control of MHD instabilities. The most basic example of this control is the regulation of the plasma vertical position with radial field feedback [25–27]; when this control is lost, the plasma can drift upwards or downwards, leading to a disruption known as a vertical displacement event (VDE). More recently, active control has been demonstrated for both the slowly varying  $n = 1$  error field [77, 78] and the rapidly growing  $n = 1$  the RWM [51, 52, 79–81]. Control of destabilized NTMs has been demonstrated with localized electron cyclotron current drive (ECCD) [72, 82–86], and NTMs have been avoided with so-called ‘preemptive ECCD’ [87].

While these active mode stabilization techniques are critical, this paper addresses the more basic question of what operating regimes result in minimal disruptivity for a high- $\beta$  spherical torus. These regimes would likely not eliminate the need for active stability control; rather, they may provide scenarios where active control have the best chance of eliminating disruptions. This is an important question in light of the wide range of operating points that have been suggested for next-step STs. For instance, in the context of

the Fusion Nuclear Science Facility (FNSF) [88] mission, candidate spherical torus designs [89–95] have  $\beta_N$  values between 3.5 and 5.2 and  $q^*$  values between 2.3 and 3.8. Clearly, empirical guidance on how these parameters impact disruptivity would be beneficial.

This paper describes (i) global parameters that lead to minimal disruptivity in NSTX [96] and (ii) some disruption causes and processes that have not been widely discussed in previous NSTX MHD publications. Section 2 discusses the analysis methods used in this paper. Section 3 describes some general statistics of NSTX disruptions. These include the disruption rate, the typical stored energies and plasma currents at the time of the disruption, and the stored energy and plasma current losses in the phase preceding the disruptions. Section 4 describes the disruptivity statistics for neutral beam heated H-mode plasmas in NSTX; the disruptivity is studied as a function of single engineering or physics parameters, and in terms of pairs of relevant parameters. Section 5 discusses the impact of  $n = 1$  RWM control on the disruptivity. Section 6 discusses some of the phenomenology of disruptions during the early flat-top phase of the discharge. Section 7 discusses disruptions at the low- $q^*$  boundary. Section 8 discusses the role of  $q_{\text{min}}$  evolving towards unity in determining the onset of often disruptive core  $n = 1$  modes, while section 9 describes the phenomenology of very high stored-energy disruptions in NSTX. Section 10 provides a summary of these results.

NSTX is a medium size spherical torus located at Princeton Plasma Physics Laboratory. The major radius of typical plasmas is  $R_0 = 0.85$  m, with aspect ratios  $R_0/a = 1.35$  to 1.55. The plasma currents are typically in the range  $600 < I_P (\text{kA}) < 1300$ , with toroidal fields between 0.35 and 0.55 T. Neutral beam heating with powers up to 7 MW, oriented parallel to the plasma current, is used for most high-performance plasmas, [97] and can be used for  $\beta_N$  control [98]. High-harmonic fast wave (HHFW) heating at 30 MHz with powers up to  $\sim 6$  MW is also available [99].

## 2. Analysis methods

Two quantities indicating the tendency of the plasma to disrupt will be considered in this paper: the disruptivity and the disruption rate. The disruptivity is defined as the number of disruptions that occur when the plasma is in a particular part parameter space, divided by the total duration that the plasma is in that state [56]. The disruptivity is thus related to the state of the plasma at any particular time, and will be studied in the context of NSTX data in sections 4 and 5. The disruption rate, on the other hand, is simply the fraction of discharges that disrupt during some part of the discharge; the disruption rate in NSTX will be briefly summarized in section 3. Of the two measures, the disruptivity is likely to be more closely related to the physics that determines the operating space.

A key question to address is the definition of disruption onset. Figure 1 shows the  $I_P$  and stored-energy ( $W_{\text{MHD}}$ ) waveforms for three different disruptions; here the subscript ‘MHD’ implies that the stored energy is computed from the reconstructed MHD equilibrium of the plasma. Two times are indicated by vertical lines in each frame. The time of the current quench ( $t_{\text{quench}}$ ) is shown in red. The current quench follows within a few ms of the thermal quench, as

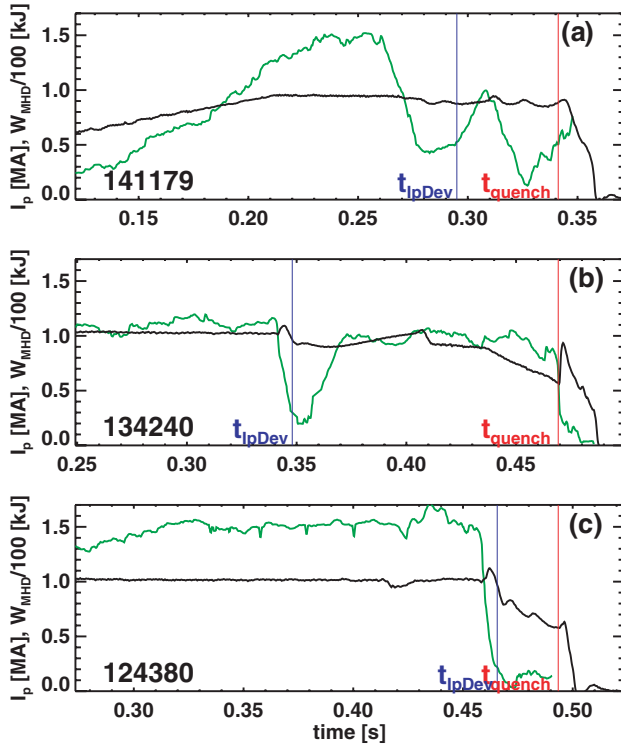


**Figure 1.** Evolution of the plasma current ( $I_p$ , in black) and stored energy ( $W_{\text{MHD}}$ , in green) for three disrupting discharges. See text for further details, and note the large current loss before the final current quench at  $t = t_{\text{quench}}$  in frames (b) and (c).

the current decays rapidly in the cold plasma. This time  $t_{\text{quench}}$  is determined automatically by the routine described in [12].

Note, however, that the plasma energy begins to decay, or shows discrete collapses, 100 ms or more before  $t_{\text{quench}}$ . Those reductions in stored energy are due to the events that trigger the disruption process (mode-lock, RWM,  $H \rightarrow L$  back transition, etc), but they are not indicative of the thermal quench itself. Indeed, the 50–150 ms that often separates the disruption precipitating event and the thermal/current quenches is typically long enough that the plasma conditions at the time of the final quenches have little resemblance to those during the time when the disruption process was initiated. For this reason, when considering the conditions that lead to a disruption, it is more relevant to consider the conditions at the times of these first stored-energy collapses.

Automatically determining the times of these collapses is quite difficult, due to the many dynamics that impact the stored energy. However, we have observed that these large thermal collapses often result in transient drops of the plasma current; this is because the non-inductive current drive sources are reduced when the poloidal  $\beta$  and fast ion content are reduced. The plasma control system then typically increases the loop voltage to restore the current to the requested value. Hence, the time of the first negative  $I_p$  deviation ( $t_{\text{IpDev}}$ ), shown as blue vertical lines in figure 1, can be used to automatically determine the time of events that begin the disruption process. The details of computing the time of first  $I_p$  deviation are given in the appendix.

Figure 2 shows a histogram of  $t_{\text{quench}} - t_{\text{IpDev}}$ . It can be seen that in most cases the  $I_p$  deviation time precedes the current

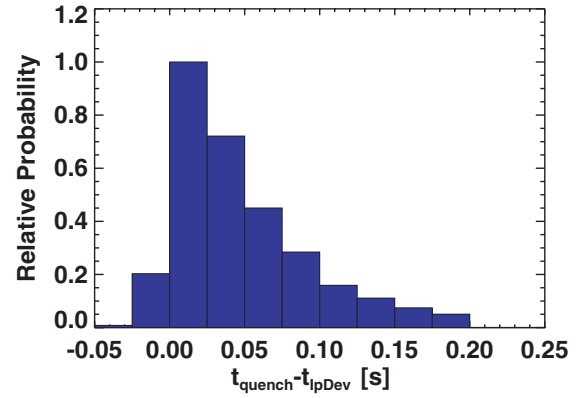


**Figure 2.** Histogram of  $t_{\text{quench}} - t_{\text{IpDev}}$ , the time between the negative deviation of  $I_p$  ( $t_{\text{IpDev}}$ ) and the time of the current quench ( $t_{\text{quench}}$ ). See text for details on the calculation of  $t_{\text{IpDev}}$ .

quench by between 0 and 0.1 s. There are a few cases where the  $t_{\text{IpDev}}$  comes after  $t_{\text{quench}}$ ; these correspond to cases where there is an  $I_p$  spike of fairly long duration but no pre-disruption current loss;  $t_{\text{quench}}$  is defined by the beginning of the spike, and is thus before the first negative deviation.

Two independent executions of the equilibrium reconstruction code EFIT [100] occur after every NSTX discharge. The EFIT01 [101] is constrained by measurements of the plasma current, coil currents, estimates of the vessel currents and poloidal field and flux measurements at discrete points along the plasma boundary. The EFIT02 [49] reconstruction is constrained by those measurements, plus the plasma diamagnetism and a loose constraint on the pressure profile from the density and temperature measured by multi-point Thomson scattering (MPTS) [102]. The EFIT02 generally produces better reconstructions and is present for the vast majority of NSTX discharges; this study only uses discharges that have this reconstruction available.

We have sampled data from every discharge in the NSTX database since 2005, with sampling time of 0.0333 s; a 3 element wide non-causal median filter is applied to the EFIT data to remove unphysical transients from the data before this sampling is carried out. The sampling time of 33.3 ms matches the minimum confinement time of a typical H-mode NSTX discharge (see figure 6 of [103]), but is longer than the typical MPTS update times or times between EFIT reconstructions. Quantities recorded on this timebase include many equilibrium properties from EFIT, the heating power from the neutral beam and HHFW heating systems, the electron temperature and density from a MPTS diagnostics, the toroidal rotation as measured by the charge exchange spectroscopy (CHERS) diagnostic [104], and the total radiated power from an array of bolometers.

In addition, the database records as best available whether there were characteristics of a discharge which make it more or less prone to disrupt. For instance, any faults reported by the computer that controls the poloidal and toroidal field coils are recorded. The amplitude and toroidal mode number of any magnetic braking [105–110] applied to the plasma are recorded, as are the status of  $n = 1$  RWM control [52, 109, 111],  $n = 1$  dynamic error field correction [78] and  $n = 3$  error field correction [112]. Also recorded are any non-standard techniques applied to the plasma, including vertical

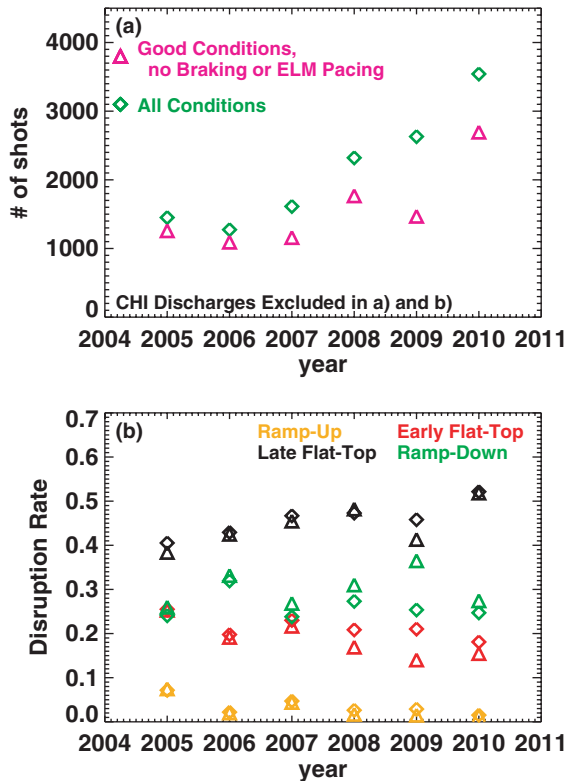


**Figure 3.** (a) The number of discharges and (b) the disruption rate, for NSTX, sorted by year. The diamonds correspond to all discharges, while the triangles correspond to discharges where the machine conditions were nominally good and neither ELM pacing nor magnetic braking were used.

jogs for ELM pacing [113], pulsed 3D fields for ELM pacing [114–116], or isoflux [117, 118] control of the divertor X- and strike-points [119, 120]; these are not necessary disruptive techniques, but a large fraction of the discharges utilizing them were for development, when the disruption rate was higher. Finally, the database records if the discharge was taken during a phase with ‘good conditions’, or during a phase of machine commissioning at the beginning of the run or with known bad vacuum or PFC conditions.

### 3. Disruption statistics and phenomenology in NSTX

Some basic statistics regarding the NSTX disruption rate are shown in figure 3. Figure 3(a) shows the total number of discharges under consideration, for the 2005–2010 run campaigns. The green points in this figure show that starting in 2008, there was a dramatic increase in the total number of discharges. This is due to the use of lithium conditioning of the PFCs [121, 122] that allows the time between discharges to be reduced to 10 min, without the between-shot helium glow-discharge cleaning (GDC) that was typical of previous NSTX operations and mandated a 15–20 min cycle time. The magenta triangles show the total number of discharges taken during phases with good conditions, and with no ELM pacing or magnetic braking. These generally track the total number of discharges, except in the 2009 campaign. Residual lithium carbonate left inside the vessel from the previous run campaign compromised the beginning of the 2009 campaign, and the

problem was only remedied by a series of noble gas glow-discharge phases, followed by helium GDC and conditioning with fresh lithium.

The disruption rate as a function of year is shown in figure 3(b), divided into four categories. The yellow points correspond to disruptions during the plasma current ramp-up. These are a very small fraction of the total number of disruptions, and their frequency has generally decreased in more recent campaigns.

The red points, labelled ‘early flat-top’, correspond to disruptions that occur within 0.25 s of the start of the  $I_p$  flat-top (SoFT). During the first 0.25 s after SoFT, the  $q = 4, 3$  and 2 surfaces enter the plasma as the current penetrates to the core. As will be discussed in more detail in section 6, instabilities at these rational surfaces often slow the plasma rotation and lock to the wall, leading to a disruption. There has been a modest reduction in disruptions during this early phase of the discharge during recent campaigns.

Disruptions during the later flat-top are shown as black points in figure 2(b). These cases correspond to disruptions that occur between 0.25 s after the SoFT, and the end of flat-top (EoFT), which is defined by either the pre-programmed ramp-down of the plasma current or the ohmic heating coil reaching its current limit. The discharge characteristics leading to disruptions in this phase of the discharge have been well documented in previous NSTX publications, and include RWMs [46, 47, 49, 52, 109, 111] sometimes caused by diminished rotation due to uncorrected error fields [78, 112],  $n = 1$  kink/tearing modes that lock to the wall [73, 103, 123–125], loss of vertical position control and  $H \rightarrow L$  back transitions driven by plasma-wall gaps becoming too small or insufficient input power. The fraction of discharges disrupting during the flat-top has increased slightly in recent years.

Finally, disruptions during the ramp-down are indicated in green. Note that NSTX did not have any automated, event-based stored energy and current ramp-down algorithm. Hence, this category include cases where the plasma current is deliberately ramped down, though typically without any ramp-down of the beam power or modifications to the shaping. It also includes the many cases where the solenoid current limit is reached during the disruption-free flat-top period. The rapid reversal of the loop voltage as the solenoid current returns to zero often results in disruption, which is classified here as having occurred during the ramp-down. In any case, disruptions during this phase of the discharge have been fairly constant over the recent run campaigns. It is likely that if more careful discharge termination strategies were developed, this class of disruption could be reduced in frequency.

We also note the apparent increase in the ramp-down disruption rate during the 2009 campaign. This can be attributed to the reduced rate of early and late flat-top disruptions during that campaign. More discharges lasted to the ramp-down phase during that campaign, increasing the disruption count during that phase. Unfortunately, the positive disruptivity trends in 2009 were not maintained for the 2010 campaign, likely due to operational complexity associated with the Liquid Lithium Divertor [126] modules.

Overall, it is clear that the disruption rate in NSTX is quite high, with the majority of shots disrupting during the pre-programmed  $I_p$  flat-top, and a small fraction of discharges

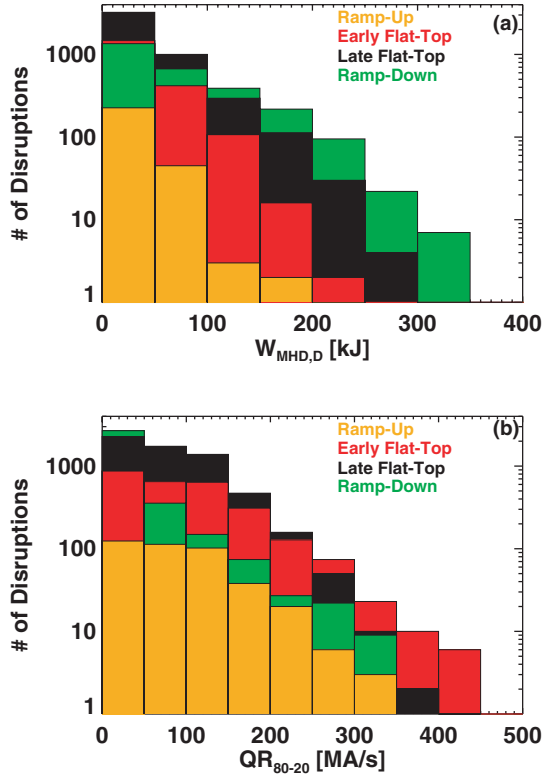


**Figure 4.** Histograms of (a) the pre-disruption stored energy and (b) the current quench rates for NSTX disruptions since 2005.

lasting through the ramp-down without disruption. We wish to note, however, that this large disruption rate has not been the barrier to scientific progress that might be assumed first. Disruptions in NSTX generally have a negligible effect on the performance of the subsequent plasma, so that the ramp-down disruptions have essentially no impact on the research program. Some of the late flat-top disruptions interfere with the goals of the discharge, but there is quite often sufficient duration previous to the disruptions for the physics goals of the discharge to be met. Only the early flat-top disruptions are uniformly detrimental to the physics program.

Having established the frequency with which disruptions occur, we now focus on some general characteristics of these disruptions. Figure 4(a) illustrates a histogram of the stored energy at the time of the current quench, and figure 4(b) shows a histogram of current quench rates. Here,  $W_{\text{MHD}}$  is the stored energy from equilibrium reconstruction, and the subscript ‘D’ implies that the measurement is made just before  $t_{\text{quench}}$ . The quench rate is defined using the ‘80–20’ definition [11]

$$QR_{(80-20)} = -\frac{0.6 \times I_{\text{PD}}}{t_{20} - t_{80}},$$

where  $I_{\text{PD}}$  is the plasma current at  $t_{\text{quench}}$  and  $t_{20}$  and  $t_{80}$  are the times when the plasma current has decayed to 20% and 80% of  $I_{\text{PD}}$ . These two quantities reflect the mechanical [15] and thermal loading [3] due to the disruptions.

With regard to stored energies in figure 4(a), we see that disruptions during the  $I_{\text{p}}$  ramp-up and early flat-top typically do not have large stored energy at times just preceding the current quench. This is not a surprise, in that the discharges have not had sufficient time to reach high values of  $W_{\text{MHD}}$

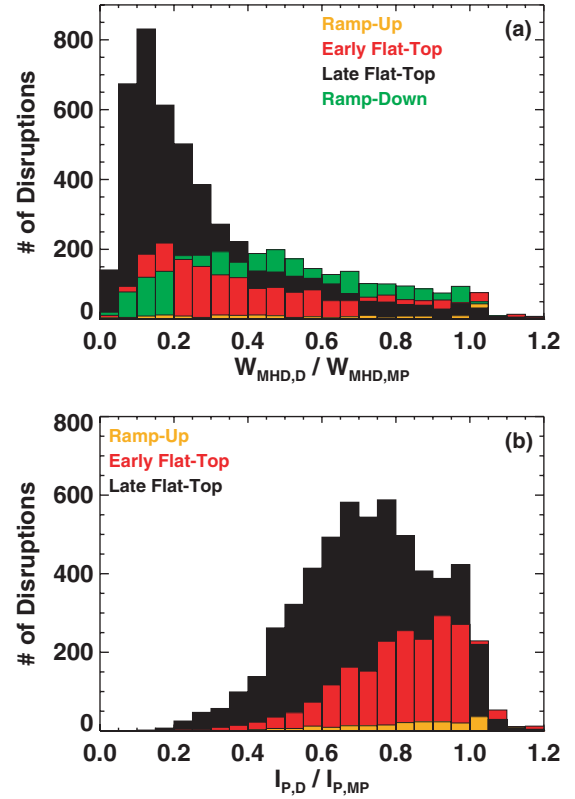


**Figure 5.** Histograms of the pre-disruption fractions of the (a) stored energy ( $W_{\text{MHD}}$ ), and (b) plasma current ( $I_{\text{p}}$ ), for disruptions since the 2005 run campaign. The subscript ‘D’ indicates that a quantity is recorded at a time just preceding the disruption current quench, while the subscript ‘MP’ implies that a quantity is recorded at the time of maximum performance (maximum stored energy in this case).

before disrupting. On the other hand, the largest stored energies at the time of the current quench are in the range of 350 kJ, and are clearly associated with disruptions during the  $I_{\text{p}}$  ramp down; the phenomenology of these disruptions will be discussed in detail in section 9. Disruptions during the  $I_{\text{p}}$  flat-top have maximum stored energy in the range of 250 kJ.

Figure 4(b) shows that fast quenches are unlikely during the disruption ramp-down and later flat-top. Rather the highest quench rates tend to occur during the early flat-top. Note that current quench rates up to  $1 \text{ GA s}^{-1}$  have been observed in NSTX during the earlier operation of NSTX [12]; however, quench rates that high have not been observed in the more recent run campaigns that contribute data to the present analysis.

As noted in the discussion of figure 1, there is often a substantial loss of stored energy, and some loss of plasma current, in the phase preceding the disruption. This loss of energy can reduce the energy conducted to the divertor during the thermal quench, while the current loss can reduce the eddy-currents driven by the current quench; both of these effects mitigate the deleterious impact of the disruption. These losses are assessed for NSTX in figure 5. Frame (a) shows the ratio of stored energy ( $W_{\text{MHD}}$ ) at the time of the disruption to that at the time of maximum performance; in this figure, the time of maximum performance is defined as the time with highest stored energy. Frame (b) shows the same ratio, but for the plasma current instead of the stored energy.

With regard to the stored-energy loss, we see that large stored-energy losses are the norm for discharges disrupting during the flat-top, and especially during the later flat-top. This is the reason why the maximum disruption stored energy during the flat-top is  $\sim 250$  kJ, despite the maximum stored energy in NSTX being  $\sim 460$  kJ [103]. Ramp-up disruptions tend to have a smaller fractional stored-energy drop, but also tend to have fairly low stored energy. On the other hand, the stored-energy loss for ramp-down disruptions is more evenly distributed, with many examples showing no pre-disruption energy loss. An example disruption in this category will be discussed in section 9.

With regard to the pre-disruption current loss, figure 5(b) illustrates results fairly similar to the trends in stored energy. The plasma current loss for disruptions during the ramp-up or early flat-top can be fairly small, with the peak in the histogram occurring at or near  $I_{p,D}/I_{p,MP}$  unity, but a large tail to small values of  $I_{p,D}/I_{p,MP}$ ; see figure 1 for examples with large current loss. Disruptions during the later flat-top tend to have a larger loss of current before the current quench.

Finally, we note that while this discussion has focused on the current quench and stored-energy loss, runaway electrons and halo currents can also cause damage to the tokamak plant during a disruption. Halo currents in NSTX have been discussed in [34], and in the spherical torus MAST in [31]. Disruption-generated runaway electrons have not been observed in NSTX.

#### 4. Disruptivity analysis for NB heated H-mode plasmas

This section examines the disruptivity in various portions of parameter space. Recall that the database includes all NSTX discharges, sampled 30 times per second. However, the data utilized in the analysis in this section do not include all of these samples. Constraints applied to the data in this section include:

- Only samples during the  $I_p$  flat-top are considered. Furthermore, if a disruption occurs immediately following the initiation of an  $I_p$  ramp-down, it is not registered as being related to the samples just preceding the ramp-down.
- The discharge must have at least 0.6 MJ of neutral beam energy injected, and at most 2.5 kJ of HHFW power. This constraint effectively restricts the database to dominantly neutral beam heated discharges. Note that most concepts for next-step ST devices utilize dominantly NB heating (in addition to fusion power), and so this data filter appears quite appropriate.
- Discharges with coaxial helicity injection (CHI) plasma initiation [127–131] are excluded from this database. The majority of CHI discharges do not have any attempt to sustain them beyond the CHI phase; they have no solenoid induction, no auxiliary heating and the plasma current seldom exceeds 300 kA [131]. In some more recent cases, solenoid induction was used to ramp a CHI initiated plasma to currents as high as 1 MA [130, 131]. However, these cases were still highly developmental, and so are not included in the database.
- Deliberate VDEs and discharges with PF-coil power supply faults are excluded. Note that these deliberate

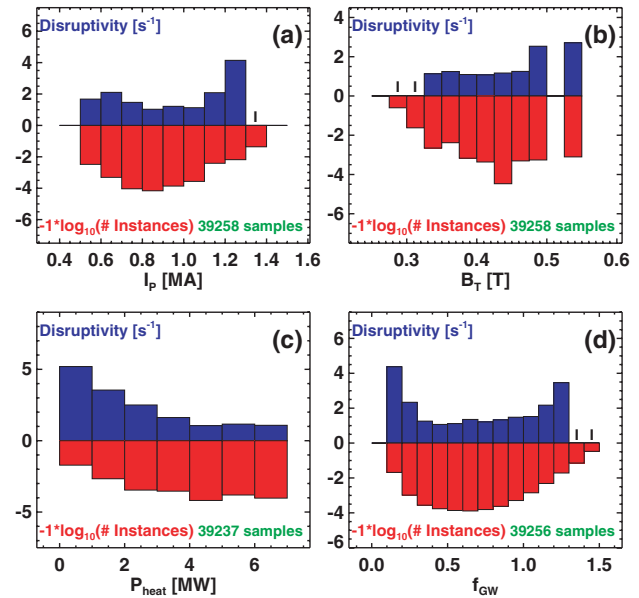


**Figure 6.** Histograms of the disruptivity (blue) and sample distribution (red) versus the engineering parameters (a)  $I_p$ , (b)  $B_T$ , (c)  $P_{\text{heat}}$  and the (d) Greenwald fraction  $f_{\text{GW}}$ .

VDEs are rare cases where the radial field feedback was intentionally frozen, allowing the plasma to drift vertically [27]. The rare events where the neutral beam power turns off pre-maturely are included in the database.

- The confinement at each sample, defined by the parameter  $H_{89}$  [132], must exceed 1.1. This constraint serves to localize the data to the high-performance phase of the discharge, and excludes samples during the low-confinement phase between  $t_{I_p, \text{Dev}}$  and  $t_{\text{quench}}$ .
- The magnetic-axis location at each sample must be within 15 cm of the vessel midplane. This excludes samples during the vertical motion of a VDE, although the period leading up to the VDE initiation is of course included.
- Only discharges during phases of a run campaign with nominally good PFC conditions are included.
- Samples during which magnetic braking is applied are excluded unless otherwise stated.

This set of constraints is sufficient to constrain the analysis to mostly neutral beam heated H-mode plasmas. However, there is no explicit test that an H-mode is achieved. Indeed, the failure to achieve H-mode is a common root-cause of disruption in NB heated discharges in NSTX. Also note that there is no sorting based on the plasma boundary shape, for instance, the elongation, triangularity, or where the plasma is single or double null.

##### 4.1. 1D Disruptivity analysis

Figure 6 shows the disruptivity statistics as a function of four primary engineering parameters in NSTX operation: (a) the plasma current, (b) the toroidal field and (c) the total input power and (d) the Greenwald fraction. The format of this figure will be used in figures 7, 9 and 10 as well. The upper blue histogram in each frame shows the disruptivity itself. The lower histogram in red shows the negative logarithm of the distribution of all samples, in order to clearly portray

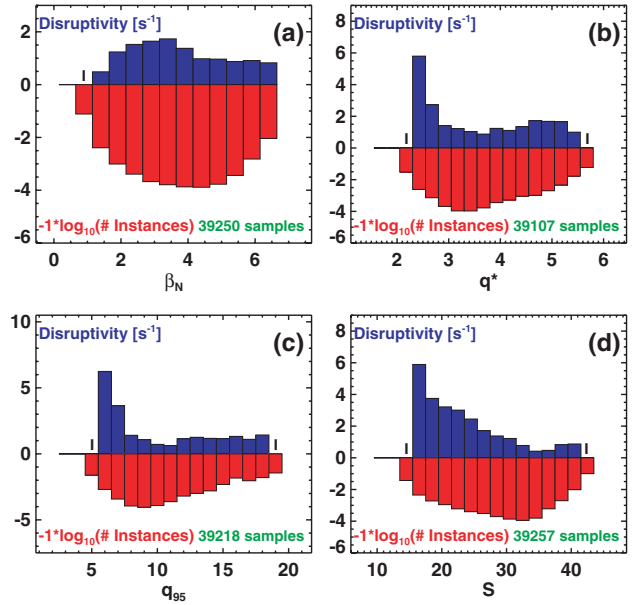
the distribution of data. There are cases in the disruptivity histograms where there is no blue bar for the disruptivity, but a finite number of samples indicated in red. In some of these cases, the number of samples in these bins was less than the minimum number (45) defined as necessary to plot in the disruptivity histograms; these cases with an insufficient number of samples are indicated with an ‘I’. In other cases, there were simply no disruptions observed for that value of the chosen parameter; these cases are indicated with an ‘N’ in the figures.

Figure 6(a) shows that the disruptivity has a minimum in the range of plasma currents  $0.7 \text{ MA} < I_p < 1.0 \text{ MA}$ . Above 1.0 MA, the edge and central safety factors tends to drop towards the values that precipitate disruption, as will be discussed in more detail below. When the disruptivity is plotted against toroidal field, we see that the disruptivity is fairly constant from 0.35 to 0.45 T. Higher toroidal fields result in prohibitively short plasma durations due to heating limits on the TF coil itself, and so operations in this regime is typically reserved for non-standard operating conditions. Examples of such non-standard conditions that contribute to a higher disruption rate include experiments designed to maximize the non-inductive current fraction at very high elongation and  $\beta_N$ , or L–H threshold experiments. Thus, the observed increase in disruptivity at higher toroidal field is likely a result of the NSTX research program. Figure 6(c) shows that there is a significant reduction in the disruptivity as the heating power is increased, an apparently paradoxical result that will be discussed in greater detail below. Finally, figure 6(d) indicates a broad region of minimal disruptivity for Greenwald fractions of  $0.35 < f_{GW} < 1.0$ , indicating that the allowable density operating range is quite broad. The increase in disruptivity above  $f_{GW} = 1$  may be related to the density limit. However, the phenomenology of those disruptions has not been verified as being similar to that of density limit disruptions in conventional aspect-ratio tokamaks.

This same analysis is repeated in figure 7, but for physics parameters thought to be indicative of tokamak and ST operational boundaries. Figure 7(a) shows the disruptivity as a function of  $\beta_N$ . Interestingly, there is no clear increase in disruptivity at the highest value of  $\beta_N$ . Indeed, the disruptivity tends to be higher for  $\beta_N < 4$  than for  $\beta_N > 4$ , though the effect is not dramatic. Of course, there is a  $\beta$  limit in NSTX. However, it cannot be easily captured by a single value of  $\beta_N$ , and it is clear that other parameters impact this limit.

In contrast, there is a clear increase in disruptivity for lower values of the edge safety factor. This is illustrated in figures 7(b) and (c), where there is an increase in disruptivity for  $q^* \lesssim 2.7$  or  $q_{95} \lesssim 7.5$ . Having the edge  $q$  above this value does not guarantee disruption avoidance, but having it drop beneath these values increases the disruption probability dramatically. This low- $q$  disruptivity boundary will be discussed in more detail in section 7.

As indicated in the introduction and implied by the discussion of figures 7(b) and (c), the plasma boundary shaping plays a strong role in determining the disruptivity. We can combine the various shaping effects (aspect ratio  $A$ , elongation  $\kappa$ , triangularity  $\delta$ ) into a single parameter known as the shape factor  $S \equiv q_{95} I_p / a B_T$ , which depends on the shape moments roughly as  $\varepsilon(1 + \kappa^2)f(\kappa, \delta, \varepsilon, \dots)$  [133]. To



**Figure 7.** Disruptivity as a function of (a)  $\beta_N$ , (b)  $q^*$ , (c)  $q_{95}$  and the (d) shape factor  $S$ .

provide some perspective on this quantity, figure 8 shows two plasma boundaries. The left double-null boundary has the highest elongation compatible with filling the vacuum chamber while leaving reasonable plasma-wall gaps, and has a shape factor of 37. Note that the outer boundary is also quite conformal to the passive plates, resulting in good coupling and wall stabilization. This shape is indicative of that used for the highest performance plasmas in the later NSTX run campaigns. The case on the right has both lower elongation and triangularity, and results in a shape factor of  $\sim 20$ . It is also more poorly matched to the outer contour defined by the passive plates. Returning to frame 7(d), we see that the disruptivity drops rapidly as the shape factor is increased, and has a minima at shape factors of 35–40. This result reinforces the role of strong shaping in facilitating high performance operations.

The plasma stability is also a function of internal profile shapes, and figure 9 shows that these dependences are reflected in the disruptivity statistics. The first quantity under consideration is the pressure peaking factor, defined as the central pressure normalized to the volume average pressure ( $F_p = p_0 / \langle p \rangle$ ). It is well documented from theory [41] and experiments at conventional [39, 134–137] and low [46, 47, 103, 138] aspect ratio that increases in the pressure peaking factor have a deleterious effect on the global stability. Figure 9(a) shows that the disruptivity is minimized for the lowest values of the pressure peaking factor, and increases up to peaking factors of about 3. The disruptivity then stays high through  $F_p = 5$ . There is some reduction in disruptivity at very high pressure peaking. This region is dominated by low- $\beta_N$  L-mode time-slices, often early in the  $I_p$  flat-top before the  $L \rightarrow H$  transition; these equilibria are not of interest as the target scenario for future ST development.

We see a similar trend in the disruptivity as a function of the internal inductance, defined as  $l_i = l_i(1) = I_p^2 \iiint B_p^2 dV / V (\mu_0 I_p)^2$ , where  $V$  is the volume of the plasma;

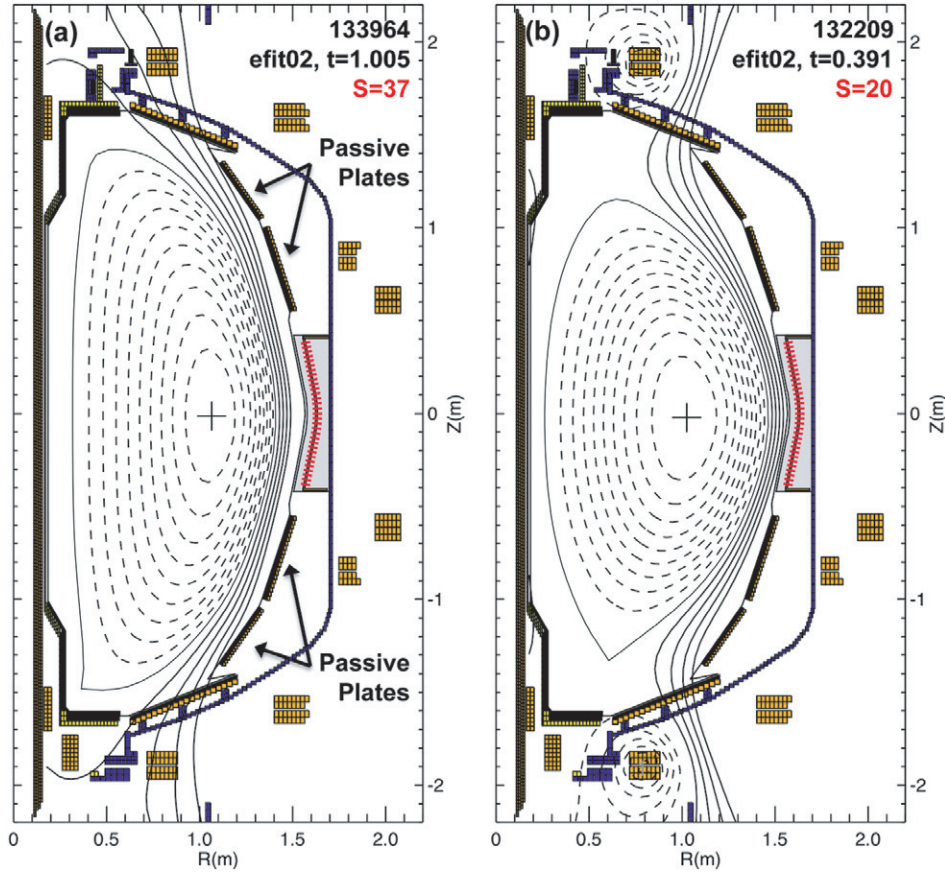


**Figure 8.** Example plasma boundaries with extreme values of the shape factor  $S$ . Frame (a) shows a strongly shaped plasma with  $S = 37$ , while frame (b) shows a weakly shaped plasma with  $S = 20$ .

this parameters is indicative of the current profile shape, with high values of  $l_i$  indicating that the current profile is more strongly peaked on axis. The minimum disruptivity occurs at low values of  $l_i$ , and increases dramatically as  $l_i$  increases. Simplistically speaking, there are at least three reasons for this trend. Firstly, the efficacy of the plasma shape and vertical position control increases when  $l_i$  is lowered, since the plasma current is then closer to the coils. Secondly, moving more current closer to the edge increases the coupling to the wall and improves the global  $n = 1$  stability in the wall-stabilized regime. Third, equilibrium and current drive calculations show that increased  $l_i$  is often associated with increases in the pressure peaking [34], which is independently associated with increases in disruptivity.

The no-wall stability limit is often quoted as being proportional to value of  $l_i$ , with ratios between 2.5 and 4 indicative of the stability limit at conventional aspect ratio [41]. However, as can be expected from figures 7(a) and 9(c) and illustrated in figure 9(c), the disruptivity in NSTX is generally lowest at high values of  $\beta_N/l_i$ , with a minima in the disruptivity at  $\beta_N/l_i \sim 12$ . The higher  $\beta_N$  limit is due to the heavier weighting of the high-field, good curvature region in the ST geometry, while the broad current profile has the benefits noted above (better shape and position control, better  $n = 1$  coupling to the wall). Finally, the combination of high- $\beta_N$  and low- $l_i$  will assist in maintaining elevated  $q_{\min}$ , thus avoiding the onset of core  $n = 1$  modes (see section 8).

Finally, we consider the disruptivity as a function of rotation in figure 10. For this analysis, we consider the rotation in both the plasma core and the midradius, and we include samples where magnetic braking was applied to the plasma. Here, the core is defined as the average of CHERS channels 4–7 spanning  $R = 0.99$  to  $1.09$  m, while the midradius is defined as the average of the CHERS channels 16–20 spanning  $R = 1.27$ – $1.34$  m; these midradius chords are in the vicinity of the  $q = 2$  surface for typical NSTX NBI heated discharges.

Figures 10(a) and (b) indicate that the disruptivity is independent of rotation over a wide range. However, we find a significant increase in disruptivity for  $F_{T,\text{core}} \lesssim 6$  kHz, or  $F_{T,\text{mid-radius}} \lesssim 3$  kHz. One reason for this trend is the tendency for rotating core  $n = 1$  modes that initiate at higher plasma rotation to slow and ultimately lock the plasma. This will be observed in figure 14 of this paper for modes early in the  $I_p$  flat-top and figure 15 for modes in the later phase of the discharge, or for later flat-top modes as described in [124, 125] and section 6.3 of [103]. The other reason for increased disruptivity at low rotation is related to the RWM.

Various papers from NSTX, DIII-D, and JT-60 have reported a threshold for RWM onset in terms of the rotation normalized to the Alfvén frequency [48, 80, 140, 141]. For instance, in looking at early NSTX data, [48] reported that the threshold was a profile quantity, and that stability was indicated by the criterion  $V_\phi \tau_A > 1/4q^2$ . Using this as guidance, the rotation data are normalized by  $F_A = V_A/2\pi R_0$



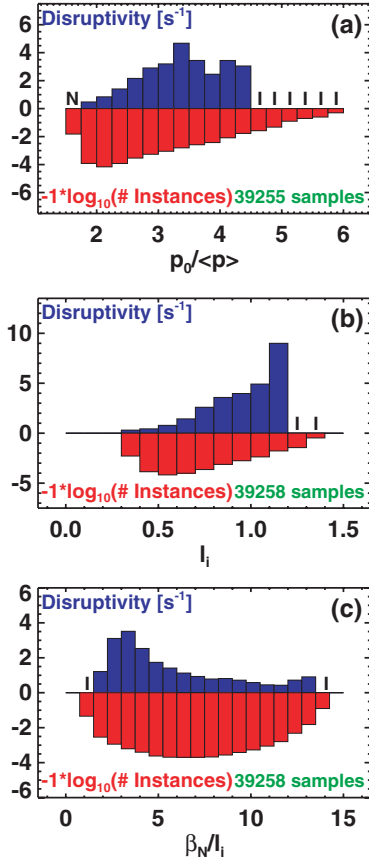


**Figure 9.** Disruptivity as a function of (a) the pressure peaking factor, (b) the internal inductance and (c)  $\beta_N/l_i$ .

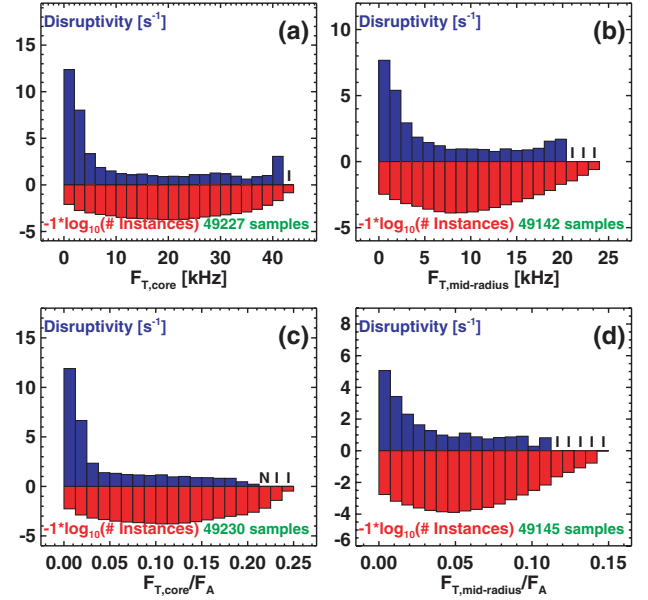
(with  $V_A = |B_0|/\sqrt{2\mu_0\bar{n}_e m_p}$ ). Here,  $|B_0|$  is the central vacuum toroidal field and  $\bar{n}_e$  is the line-average density. The disruptivity is plotted as a function of normalized rotation in figures 10(c) and (d). We find that, in an approximate sense, the disruptivity increases for  $F_{T,core}/F_A < 0.03$  or  $F_{T,mid-radius}/F_A < 0.02$ .

#### 4.2. 2D Disruptivity analysis

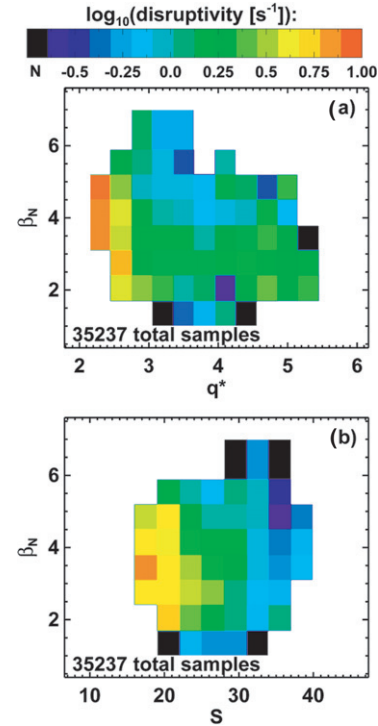
In this section, we consider the 2D plots of the disruptivity versus  $\beta_N$  and an additional parameter, with the goal of determining additional correlations not present in the 1D histograms of section 4.1. The constraints applied to the data are those in the bulleted list at the beginning of section 4. The minimum number of samples in any of the 2D bins is 25. Bins with no disruptions are coloured black, as indicated by the ‘N’ under the colourbar.

Figure 11(a) shows the disruptivity as a function of  $\beta_N$  and  $q^*$ . It is clear that operation at low  $q^*$  increases the likelihood of disruption for essentially all  $\beta_N$ , but that this likelihood is largely independent of  $q^*$  for  $q^* \gtrsim 3$ . This plot also shows that there is a broad region of low disruptivity in the vicinity of  $\beta_N = 6$  and  $q^* = 3.5$ . The same disruptivity data are plotted against  $\beta_N$  and shape factor  $S$  in figure 1(b). This figure shows a strong region of minimum disruptivity at high  $\beta_N$  and strong shaping.

The disruptivity is plotted as a function of  $\beta_N$  and profile parameters in figure 12. This figure shows that the disruptivity



**Figure 10.** Disruptivity plotted against (a) the core and (b) midradius rotation. Frames (c) and (d) show the same data, normalized to the Alfvén frequency. See text for additional details.



**Figure 11.** Disruptivity as a function of  $\beta_N$  and (a) the cylindrical safety factor  $q^*$ , or (b) the shape factor  $S$ .

is comparatively low for all  $\beta_N$  when  $F_P$  (figure 12(a)) and  $l_i$  (figure 12(b)) are sufficiently low. In both cases, there is an increase in disruptivity when the profiles become more peaked (larger values of  $p_0/\langle p \rangle$  or  $l_i$ ), and that the highest disruptivity occurs with peaked profiles and higher  $\beta_N$ . Note that there is a small region of reduced disruptivity at higher  $F_P = p_0/\langle p \rangle$ , but low  $\beta_N$ . This region explains why the 1D disruptivity in figure 9(a) does not increase monotonically with  $F_P$ .

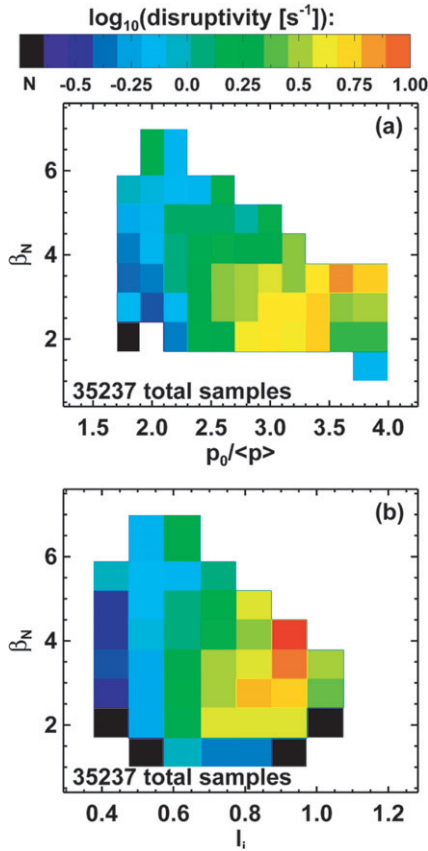


**Figure 12.** Disruptivity as a function of  $\beta_N$  and (a) the pressure peaking factor, or (b) the internal inductance.

#### 4.3. Discussion of disruptivity

The figures in this section demonstrate that within the NSTX data, there is a window of minimum disruptivity at high- $\beta_N$ , with strong shaping and broad pressure and current profiles. However, the data in figure 3 indicate that a large fraction of discharges disrupt during the later flat-top, during the high- $\beta$  phase. The reason for this is that the optimal profiles and boundary shape were typically not maintainable in NSTX. Reasons for deviation from the optimal operating points include:

- *Current diffusion.* Many NSTX discharges had current profiles that evolve through the  $I_p$  flat-top period, with  $q_{\min}$  approaching 1 (the current redistribution time in these discharges is typically 200–300 ms). When this occurs, rotating  $n = 1$  kink/tearing instabilities often onset [103, 123–125]. These instabilities always result in significant confinement degradation, and often lock to the wall, leading to disruption. These modes will be discussed in greater detail in section 8.
- *Kinetic profile evolution.* The density in NSTX discharges typically ramps continuously through the discharge. In discharges without lithium conditioning, this evolution is due to an increase in the deuterium concentration. This density rise often resulted in MARFE formation, with a resulting degradation of the edge pedestal. Under ELM-free conditions [142–144] created by lithium conditioning, the accumulation of carbon results in an

increase in the electron density. MARFE formation was typically eliminated in these cases [145]. However, the steady impurity accumulation in those scenarios resulted in large increases in  $Z_{\text{eff}}$  and radiated power, both of which eventually result in a deviation from the desired high-performance operating point.

- *Actuator or plasma control failure.* NSTX high-performance H-mode discharges are extremely sensitive to the loss of auxiliary power input, with H  $\rightarrow$  L back transitions and disruption typically following within 100 ms of sudden termination of the neutral beam power. Similarly, boundary shape control errors that result in plasma-wall gaps becoming too small often result in H  $\rightarrow$  L back transition and disruption. Note that most high-elongation, high-performance discharges in NSTX were run without closed-loop X-point height control. This often resulted in the X-point approaching the divertor floor late in the discharge due to uncompensated leakage flux from the ohmic solenoid coil.
- *Transient MHD events.* Transients such as edge-localized modes (ELMs) or energetic particle modes (EPMs) can trigger larger MHD instabilities that lead to disruptions. This triggering can be by direct coupling to the global mode, or by changes to the thermal or fast ion profiles leading to global mode instability. Further examples of this type are described in section 8.

#### 5. Impact of $n = 1$ control on the disruptivity at high- $\beta_N$ .

The discussion above has indicated that with proper shaping of the plasma boundaries and broad pressure and current profiles, it is possible to significantly reduce the disruptivity at high- $\beta_N$ . An additional mechanism for disruptivity reduction is the proper correction of non-axisymmetric error fields and feedback on RWMs.

During experiments in 2007 and 2008, a general recipe for  $n = 1$  dynamic error field correction and RWM feedback was determined via two different methods. In the first method [78], a small  $n = 1$  error field was applied, which was then amplified by the high- $\beta$  plasma, leading to rotation damping and RWM driven disruption. The feedback system was then used to apply an  $n = 1$  field proportional to the detected plasma amplified  $n = 1$  perturbation (the direct coupling of the error field coils to the sensors was removed before the feedback field was determined). There was a preferred phase between the detected field and the applied  $n = 1$  field which resulted in the near cancellation of the original pre-programmed  $n = 1$  currents and an extension of the pulse length. This feedback phase and associated feedback amplitude were then used for dynamic error field correction in subsequent discharges without the seed  $n = 1$  field.

In related experiments, rapidly growing RWMs were generated without the use of applied  $n = 1$  fields, though  $n = 3$  magnetic braking was sometimes used. The  $n = 1$  feedback phase and amplitude were then scanned in order to determine the parameters that resulted in best suppression of the rapidly growing mode [109, 111]. The amplitude and phase so determined were quite similar to that determined from the dynamic error field correction experiments, as expected

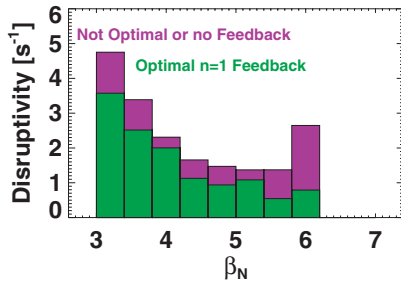


**Figure 13.** Disruptivity as a function of  $\beta_N$ , sorted by whether feedback-based  $n = 1$  control was applied. These data are for the 2007–2009 experimental campaigns. See text for additional details.

given that the plasma amplified error field should have the characteristics of the marginally stable RWM [140, 146, 147].

Previous publications have compared individual discharges with and without  $n = 1$  control: see for example [52, 78, 109, 111]. However, the statistical improvements to performance have been less well addressed. Hence, figure 13 shows the disruptivity as a function of  $\beta_N$ , for discharges with the optimal  $n = 1$  error field correction, and for discharges which do not have such correction. This figure includes data from the 2007 to 2009 run campaigns, during which there was considerable operation both with and without  $n = 1$  control. Data from the 2010 campaign, which used  $n = 1$  control for virtually all beam heated discharges and had a major change to the PFCs in the form of the Liquid Lithium Divertor, are excluded from the figure.

It is clear that the use of  $n = 1$  control improved the discharges; in particular, for any given  $\beta_N$ , the disruptivity was reduced. Of course, the use of these systems did not eliminate all disruptions. For instance, the core rotating  $n = 1$  modes to be discussed in section 8 are not eliminated by the use of this system. Furthermore, disruptions originating from  $H \rightarrow L$  back transitions or the rare hot-plasma VDE are not prevented. Finally, even with RWM control on,  $n = 1$  global modes can become unstable, if the eigenfunction becomes more internal near the ideal wall limit or if the plasma becomes strongly unstable due to loss of beneficial kinetic stabilization effects [148–154]. However, no systematic study of the loss of  $n = 1$  control in the presence of  $n = 1$  feedback has been carried out. With these caveats, it is clear that the  $n = 1$  control system was quite useful in reducing disruptivity. It appears likely that future STs should have at least some capability to use dynamic error field correction [77, 78] to maintain the beneficial plasma rotation, if not the capability for fast feedback on unstable modes.

## 6. Phenomenology of early-flat-top disruptions

It was noted in section 3 that approximately 20% of discharges disrupt during the early flat-top period, when the various rational surfaces are still entering the plasma. A spectrogram and example waveforms for a common disruption type in this category is shown in figure 14. The spectrogram and toroidal mode decomposition of  $\text{dB}/\text{dt}$  in figure 14(a) shows a series of  $n = 1$  and  $n = 2$  chirping instabilities before  $t = 0.2$ . An  $n = 1$  mode at approximately 15 kHz forms at about 0.22 s, but vanishes by  $t = 0.25$  s. A second larger

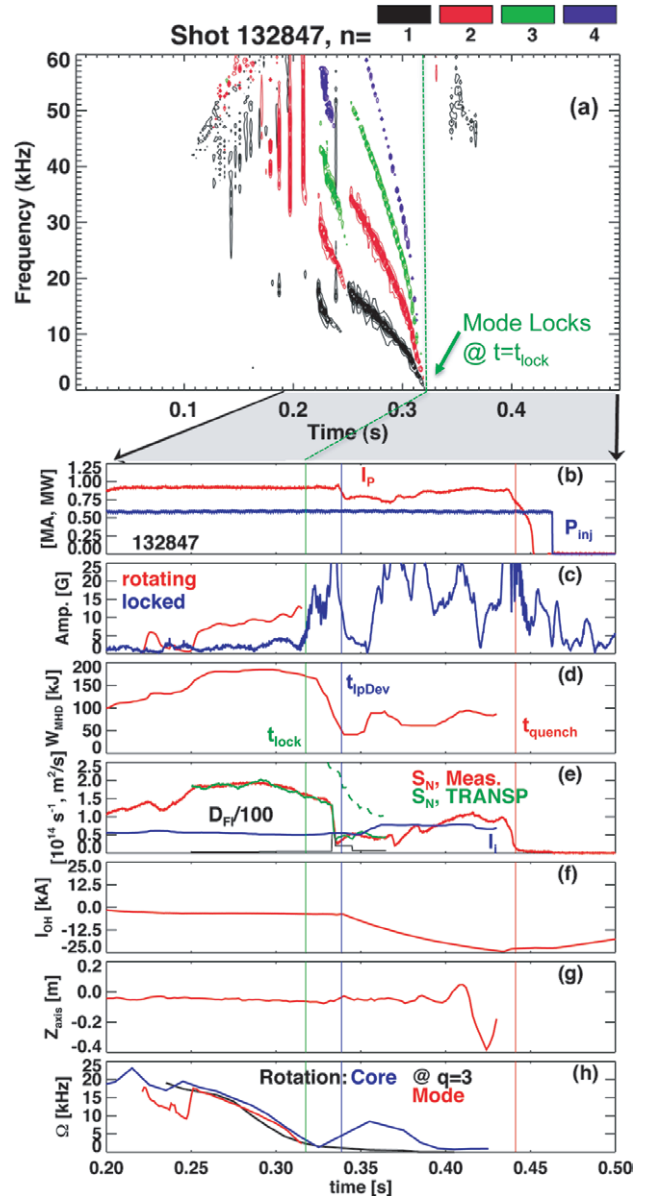


**Figure 14.** (a) Spectrogram and toroidal mode decomposition for a discharge that disrupts in the early flat-top due to MHD modes locking to the wall. Following are waveforms for (b) the plasma current and heating power, (c) the rotating and stationary mode amplitude, (d) the plasma stored energy, (e) the measured neutron emission ( $S_N$ ), neutron emission predicted by TRANSP and NUBEAM with (solid) and without (dashed) an imposed anomalous fast ion diffusivity  $D_{FI}$ , and internal inductance, (f) the solenoid current evolution, (g) the plasma vertical position, and (h) the rotation frequency in the core and at  $q = 3$ , as well as the mode rotation frequency. Note that the time-scales are different in the top frame compared with the other frames.

$n = 1$  mode is formed at about  $t = 0.25$  s. The frequency of this mode decreases continuously, ultimately dropping to zero rotation. Analysis of soft x-ray, reflectometer and magnetics data indicates that these low frequency modes originate as kink instabilities [155].

The waveforms for this discharge are shown in the bottom time traces of figure 14. Figure 14(b) shows the plasma current and heating power. The times  $t_{\text{quench}}$  and  $t_{p,Dev}$  are indicated as

vertical lines, and indicate that there is a long period between the first  $I_p$  deviation and the current quench. Figure 14(c) shows the signatures of the MHD activity that precipitate this disruption. The red curve shows the amplitude of the rotating mode that eventually locks. This signal vanishes when the mode locks at  $t = 0.32$  s (indicated by a green vertical line), and is replaced by the rapidly growing locked  $n = 1$  mode signature in blue. The stored energy in figure 14(d) begins to drop rapidly once the stationary mode begins to grow; this is partially due to an H–L back transition that occurs at  $t = 0.325$ , resulting in the loss of the edge pedestal, as well as degradation in the core confinement.

Also see in red in figure 14(e) the very rapid loss of neutron emission. It has previously been noted that because the neutron rate is largely proportional to the fast ion density in NSTX [156], these rapid drops are indicative of a large loss of fast ions. This is demonstrated in the present case by the calculation of the expected neutron emission, using the NUBEAM [157] code within TRANSP [158]. The dashed green line shows the predicted neutron emission using classical fast ion physics only, in an axisymmetric equilibrium with the measured plasma shape and position, density, temperature and  $Z_{\text{eff}}$ ; this curve clearly over-predicts the neutron emission. The solid curve shows the emission predicted when an artificial, spatially uniform but time-varying, fast ion diffusion  $D_{\text{FI}}$  is added in order to artificially mimic the actual fast ion loss mechanisms. The waveform of the fast ion diffusion is shown in black, and has an anomalous diffusion level of  $\sim 4 \text{ m}^2 \text{ s}^{-1}$  during the phase where the  $n = 1$  mode is rotating, and a 3 ms long transient at  $D_{\text{FI}} = 55 \text{ m}^2 \text{ s}^{-1}$  at the time of the neutron collapse. The emission predicted this way matches the data well, and demonstrates that some anomalous fast ion loss process occurs at this time.

The mode locking and severe confinement degradation is followed by a new set of plasma dynamics. Figure 14(e) shows that the internal inductance increases significantly in this L-mode phase, as the inductive currents, which can rather rapidly penetrate to the axis, become dominant in the low- $\beta$  plasmas. This is reflected in the much more rapid ramp of the solenoid current  $I_{\text{OH}}$  after the mode locks; the solenoid current eventually reaches its current limit of  $-24$  kA, and begins to return to zero. The large disturbances and increased internal inductance result in rapidly growing vertical motion in figure 14(g), which the vertical position control system is unable to stabilize. Discharges of this type typically disrupt when either (i) the loop voltage is reversed when the solenoid current begins to ramp to zero or (ii) uncontrolled vertical motion result in the plasma being driven into the divertor; in the present case, it appears that the vertical motion precipitates the final disruption. Finally, note that while this discharge comes from an early flat-top disruption, the events are generally representative of the sequence of RWM or mode-lock disruptions at higher  $\beta_N$  later in the flat-top.

Additional dynamics of the locking itself are shown in figure 14(h). The core plasma rotation is indicated in blue, while the rotation frequency at the  $q = 3$  surface is shown in black. Initially, the  $q = 3$  surface is rotating much more slowly than the core, as it is at fairly large minor radius when it first enters due to the strong reversed shear and peaked rotation profile. The red curve shows the frequency of the dominant

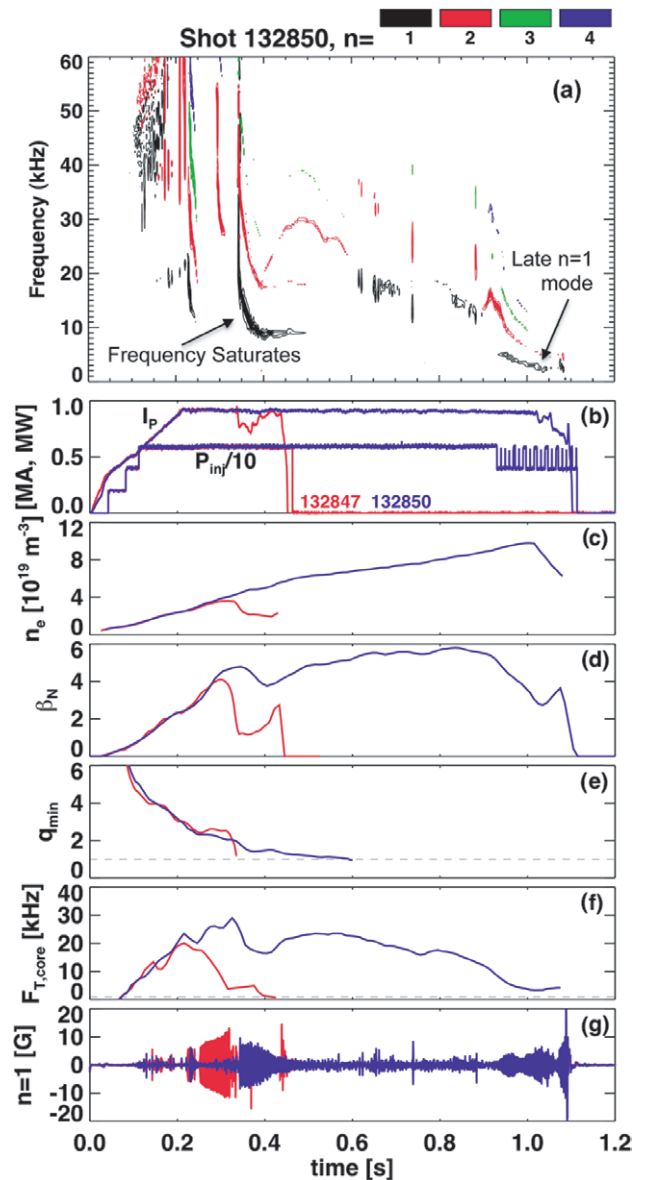


**Figure 15.** (a) Spectrogram for a discharge that avoids an early disruption through modification of the gas fuelling. Also shown are comparisons of (b) the plasma current and heating power, (c) the line-average density, (d) the normalized  $\beta$ , (e) the minimum safety factor, (f) the core toroidal rotation and (g) the  $n = 1$  MHD activity, for the stable discharge (132850) and the unstable discharge in figure 14.

low-frequency  $n = 1$  mode perturbation. The large  $n = 1$  mode strikes at  $t \sim 0.25$  s, with a frequency equal to that of the  $q = 3$  surface. This mode leads to rapid rotation damping, and the mode and plasma rotation frequencies rapidly go to zero.

This type of disruption, with rotating MHD modes that slow and lock to the wall, is among the most common for early flat-top disruptions. When discharges disrupt in this fashion, the most common control room response is to modify the early gas fuelling. This change does not necessarily eliminate the mode, but the locking to the wall can typically be avoided.

An example of this behaviour is given in figure 15, where a discharge taken shortly after that in figure 14 is illustrated. In this case, the discharge in figure 14 was fuelled using

supersonic gas injector [159] located on the low-field side of the device, while that in figure 15 used high-field side fuelling [160], entering the plasma at about 70 ms. We note, however, that similar sensitivity is observed to changes in the amount of gas injected from the high-field side. Figure 15(a) shows the spectrogram for the second discharge, while figures 15(b)–(g) show a comparison of some characteristic waveforms between the two discharges under discussion.

Considering figure 15(a) first, we see that the early MHD modes are not eliminated in the second discharge. However, their frequency evolution is modified, and no mode frequency drops beneath 10 kHz; this is sufficient to prevent the disruption. Figure 15(b) illustrates that the current ramp and injected power are similar, while figures 15(c)–(e) shows that the evolution of the line-average density,  $\beta_N$  and  $q_{\min}$  are also similar until the large mode strikes at  $t = 0.25$  s in discharge 132847. Figure 15(f) illustrates the rapid rotation damping associated with that mode. Note that the more successful discharge (132850) also has a large mode at  $t = 0.38$  s, resulting in substantial rotation damping. However, the discharge is able to survive this damping and enter a high-performance phase.

The exact details of how the early gas fuelling impacts the mode stability and rotation damping has not been established. A reasonable hypothesis is that the gas fuelling changes result in small modifications to the edge temperature, and thus resistivity. There may also be changes in the characteristics of the early chirping modes that are visible at greater than 30 kHz in figures 14(a) and 15(a); these may change the fast ion current profile. These two effects in turn impact the radius of and magnetic shear at the rational surfaces when they enter the plasma, which can impact the amplitude and spatial distribution of MHD instabilities that form. However, the detailed MHD calculations required to validate this hypothesis have not been attempted.

Finally, we note that discharge 132850 has a second  $n = 1$  mode that grows starting at  $t \sim 0.93$  s. This mode results in a substantial reduction in  $\beta_N$ , and large rotation damping. The impact of this type of  $n = 1$  mode on the safe operating space will be discussed in section 8.

## 7. Disruption causes at the low- $q^*$ boundary

We begin this section by examining figure 16, which shows the value of  $q^*$  averaged over the  $I_p$  flat-top, as a function of the  $I_p$  flat-top duration. Here, the  $I_p$  flat-top is defined as all times in the discharge where  $I_p$  is greater than 85% of the maximum value. The colours are indicative of the year during which the discharge occurred, with black points corresponding to earlier NSTX operation that is not included in the disruptivity analysis in sections 4 and 5.

First, note that NSTX operation at very low  $q^*$  is achieved, with values as low as  $q^* = 1.3$  recorded in the database. However, these discharges are extremely short, often with essentially no recognizable flat-top. This confirms that the NSTX data set is at least consistent with the idea of a ‘hard’ MHD stability limit at  $q^* \sim 1.3$ , as anticipated from ideal MHD theory. The pulse durations increase significantly as  $q^*$  is then raised, with pulses of  $\sim 1$  s duration occurring for  $q^* \gtrsim 2.7$ .

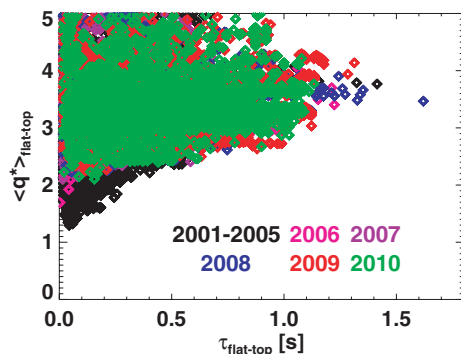


**Figure 16.** The flat-top average of  $q^*$ , plotted against the flat-top duration, for the complete NSTX database.

We also see that operation at very low values of  $q^*$  was most common in the early years of NSTX operations. Those campaigns had significant run time dedicated to achieving very high toroidal  $\beta$  values, which, by Troyon scaling, are best achieved at higher  $I_p/B_T$ , and thus low  $q^*$ . High values of  $\beta_T$  were achieved [13, 161], but for only very short duration. In later years of NSTX, more emphasis has been placed on achieving sustained high values of the non-inductive fraction [103, 125, 162, 163] or  $\beta_N$  [78, 109, 111]. As a consequence, there were few or no attempts to access this very low- $q^*$  regime during the run campaigns used for disruptivity analysis in section 4.

Hence, while we find that while equilibria with  $q^*$  as low as 1.3 have been transiently generated, we find an *operational* disruptive  $q^*$  limit roughly defined by  $q^* < 2.5$ . We have examined a number of these disruptions at the operational low- $q$  boundary during the 2005–2010 campaign, and indicate some of the disruption causes below.

- The early rotating MHD modes described in the previous section are a significant source of disruptivity at low  $q^*$ . We observe many instances of these modes locking to the wall and leading to disruption. Additionally, we observe many cases where the rotation braking associated with these modes apparently leads to onset of subsequent disruptive instabilities. It is clear that optimization of the current ramp phase of the discharge is especially important for achieving reliable operation at low- $q^*$ .
- It has been documented that the L  $\rightarrow$  H threshold power in NSTX has positive scaling with plasma current [164–166], unlike the widely accepted conventional aspect-ratio scaling  $P_{\text{LH}} = 0.0488 n_{e20}^{0.72} B_T^{0.8} S_A^{0.94}$  [167]. This results in a significant fraction of high-current discharges failing to reach H-mode, or succumbing to H  $\rightarrow$  L back transitions early in the discharge. These discharges typically then disrupt at fairly low  $\beta_N$ , due to the reduced stability of configurations with high values of the pressure peaking factor (see figures 9 and 12).
- NSTX has observed an improved confinement mode known as the enhanced pedestal H-mode (EPH-mode) [168]. In most EPH cases, the discharge transitions to H-mode in the standard way; an ELM then follows triggering the transition to the EPH configuration. The occurrence of these confinement transition increases at higher plasma current, or low  $q^*$ . However, these low- $q$  EPH scenarios

are typically short lived, resulting in disruption soon after the confinement transition [169]. The exact cause of these disruptions in EPH modes is under investigation.

- Finally, an additional cause of disruption at low  $q^*$  is the onset of core  $n = 1$  MHD activity as the central safety factor approaches unity. These modes can onset at any value of  $q_{95}$  if  $q_{\min}$  becomes low enough. However, the large inductive component at high current more often leads to the rapid onset of these modes, which are the subject of the next section.

## 8. Onset of core $n = 1$ activity

The previous sections noted that long-lived core  $n = 1$  modes, rotating with the plasma, often occur in NSTX. These modes were first documented in [123, 124], where it was shown that the modes had a large  $m/n = 1/1$  core kink component. They were shown to be responsible for the redistribution of fast ions and braking of the plasma rotation. Various saturation mechanisms for the mode were discussed.

References [73, 74] studied a class of  $m/n = 2/1$  magnetic islands, and showed that they had many characteristics of 2/1 NTM. Reference [73] showed that these modes could be triggered by EPMS [170] or ELMs [171], or grow without any obvious trigger, and that their onset was correlated with rotation shear at the  $q = 2$  surface. It was also noted that there was often a large 1/1 core kink present simultaneously with the island. This coupled 2/1 + 1/1 mode was reconstructed from soft x-ray emission data in [103, 125], and its impact on the core plasma was discussed in [103]. See [103, 123–125] for additional information on the impact of these modes on NSTX plasmas.

These NSTX modes were studied numerically with the PEST-1 [172] and M3D [173] codes in [174]. It was shown that these modes became linearly unstable as  $q_{\min}$  approached 1. Non-linearly saturated states with both 1/1 ideal displacements and 2/1 magnetic islands were observed.

In the context of this work, the question is to understand how these instabilities constrain the ‘safe’ operating regime in NSTX. To this end, a database of 138 discharges with these core MHD modes has been formed, using data from the 2008–2010 operating campaigns. These discharges have had their equilibrium calculated with the LRDFIT equilibrium reconstruction code [124]; these reconstructions are constrained by external magnetics and coil currents, pitch angle data from a motional Stark effect diagnostic [175], and the requirement that the magnetic surfaces be isotherms. The database records various equilibrium properties at time at mode onset ( $q_{\min}$ ,  $q_0$ ,  $\beta_N$ ,  $l_i$ ,  $\dots$ ), the plasma rotation frequency at the  $q = 2$  surface, and the initial mode frequency.

Also recorded in the database is information about the various trigger types, indicated by the symbol colours in figure 17. Triggerless cases are indicated in black; these discharges show the  $n = 1$  Mirnov coil amplitude growing smoothly from the background without any clear triggering disturbances. Cases with various triggering perturbations are shown in red. The ELM triggered cases have a clear ELM at the time of the  $n = 1$  mode onset, and typically show the mode frequency sweeping up from slower than the  $q = 2$  rotation at trigger time, to being equal to the  $q = 2$  rotation frequency

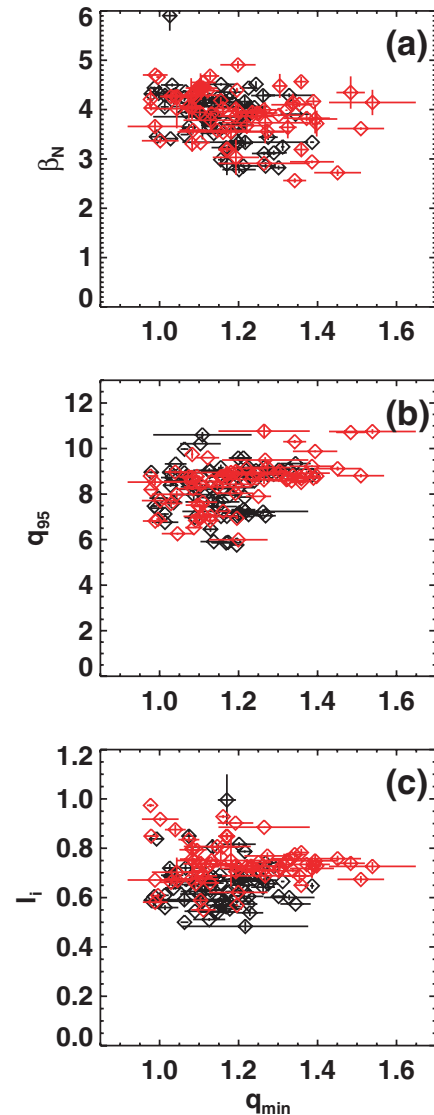


**Figure 17.** Values of  $q_{\min}$  at core  $n = 1$  mode onset, plotted against (a)  $\beta_N$ , (b)  $q_{95}$ , and (c)  $l_i$ . Red symbols are for triggered modes, while black cases are for modes that onset without a clear trigger.

some tens of milliseconds later. The EPM triggered cases show a clear high-frequency burst at the time of the mode onset, as well as a rapid drop in the neutron emission. Finally, there are a small fraction of cases in the ‘triggered’ category where EPMS and/or ELMs are present, but it is not possible to correlate the mode onset with any individual event.

The values of  $q_{\min}$  at mode onset are shown in figures 17(a)–(c), plotted against various other equilibrium parameters. Figure 17(a) shows that these modes can onset over a wide range of  $\beta_N$ , from values around 2.75 to greater than 5.0. This spans from well under the no-wall  $\beta_N$  limit, to well above that limit. The range of  $q_{\min}$  at mode onset, however, is fairly restricted, with almost all modes striking with  $1.0 < q_{\min} < 1.25$ . Figure 17(b) shows the values of  $q_{95}$  and  $q_{\min}$  at mode onset. We see that while the range of  $q_{\min}$  is rather restricted, the values of  $q_{95}$  range from 6 up to 11. Finally, figure 17(c) shows that values of  $q_{\min}$  and  $l_i$  at mode onset; we choose this because  $l_i$  was previously shown to be a rough indicator of tearing onset the ITER-similarity discharges

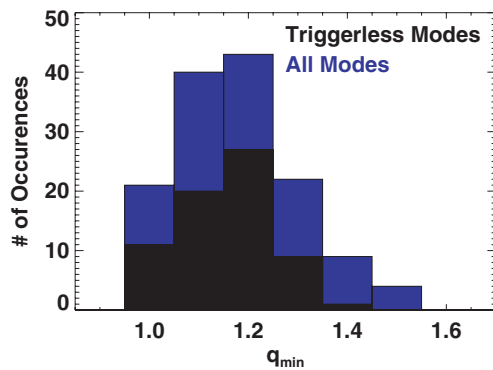


**Figure 18.** Histogram of the values of  $q_{\min}$  at the time of core  $n = 1$  mode onset, for the full 138 discharge database, and for the discharge subset with no clear trigger.

in DIII-D [176]. In this case, however, the modes onset with a very broad range of  $l_i$  values, ranging from 0.5 all the way to 1.0. From these studies, we infer that  $q_{\min}$  is the best single parameter indicator of the mode onset conditions.

A histogram of the  $q_{\min}$  values at mode onset is shown in figure 18. The complete data set is plotted in blue, as well as a subset for those cases in which the modes onset in otherwise quiescent phases with no clear triggering disturbance. For the complete data set, we see a strong peak in occurrences for  $1.0 < q_{\min} < 1.3$ , with values trailing off to values as high as 1.5.

The triggerless cases are restricted to somewhat lower values of  $q_{\min}$  though values up to  $q_{\min} = 1.4$  have been observed. The peak of the histogram is located in the vicinity of 1.1–1.2. At these low  $q_{\min}$  values, it appears that the ideal MHD onset mechanisms for the  $m/n = 1/1$  modes discussed in [174, 177–180] are likely at play. For the few triggerless cases at higher  $q_{\min}$  it is possible that there is some trigger mechanism not observable in the data.

The details of the mode physics, however, are not the purpose of this paper, which is interested in determining regions of safe operations windows. From these figures, we infer that operations with  $q_{\min}$  beneath  $\sim 1.25$  will likely be prone to core  $n = 1$  MHD modes. If the spectrum of disturbances from ELMs and EPMS (and possibly other perturbations as well) is eliminated, then operation with  $q_{\min}$  not significantly above 1.3 may be acceptable. On the other hand, if these perturbations are not eliminated, then operation with  $q_{\min} > 1.5$  may be more appropriate. We also note in passing that EPMS have previously been implicated in the triggering of NTMs in ASDEX-Upgrade [181] and RWMS in DIII-D and JT-60 [182]. Similarly, ELMs have been indicated in the triggering of the dangerous 2/1 NTM in DIII-D [183] and JET [184], RWMS in DIII-D [80] and core  $n = 1$  kink modes in JET [185]. Hence, we conclude that the sensitivity of the global stability to nominally small perturbations is not a feature unique to the ST.

In the context of disruptivity, these modes do not typically lead to prompt disruption. Rather, as indicated in [103, 123, 124], or figure 15, these modes typically grow to fairly large amplitude over a period of tens of milliseconds, during which time they can be easily detected. The sole exception to this statement are the modes triggered by EPMS,

which, as inferred from the Mirnov sensor signal, can be struck at fairly large amplitude. Once the mode becomes large, it begins to damp the plasma rotation, another easily detectable mode signature. It is only when the plasma rotation drops sufficiently for the mode to lock to the wall does the disruption typically occur. Thus, there should be sufficient time before a disruption to detect the mode and instigate some mitigating control response. The details of an appropriate control response are beyond the scope of this work.

We also wish to note that a similar  $n = 1$  core mode has been observed in MAST [178, 179]. These modes are similar in that they have strong  $m/n = 1/1$  components that onset as  $q_{\min}$  approaches unity. However, those modes in MAST are distinguished by a lack of any measurable reconnection and island formation, and their onset frequency is close to that core rotation frequency. As described in [73, 103, 125], the NSTX modes do have a tearing component, and their frequency is a better match to the rotation at the  $q = 2$  surface. Hence, while these modes may share some similarities with those observed in MAST, they also have significant differences.

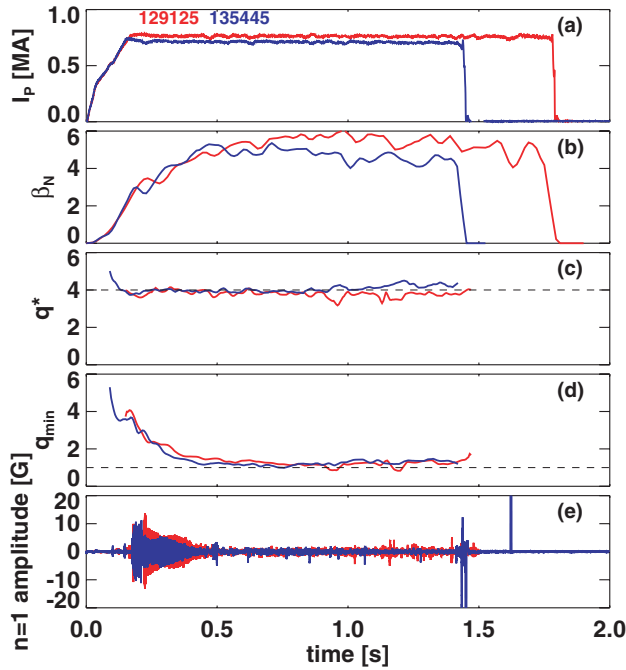
The data in figure 18 explain part of the reduction of disruptivity with power and  $\beta_N$  observed in figures 6 and 7. Increasing  $\beta_N$  will tend to raise the bootstrap current, which scales roughly as  $I_p q_{95} \beta_N$ . The bootstrap current is peaked off axis, which contributes to raising  $q_{\min}$  and avoiding these instabilities. Furthermore, the slowed current evolution with higher power and  $\beta_N$  will delay the approach to unstable  $q_{\min}$  values. However, we wish to note that although operation with  $q_{\min} \lesssim 1.2$  is clearly more prone to the onset of these modes, many examples exist with long durations of operation with  $q_{\min}$  in this ostensibly dangerous range, and without these modes striking. An example pair of such discharges is shown in figure 19; note that discharge 129125 was previously discussed in [78, 103], while discharge 135445 was previously discussed in [103, 125].

Figure 19(a) shows that these 700 and 750 kA discharges last for up to 1.5 s, corresponding to 5–7 current relaxation times. They operate at high values of  $\beta_N$  and  $q^*$ , the latter due to both the somewhat low current values and the high elongations (not shown). Figure 19(d) shows that the central safety factor hovers just above unity for at least 1 s in these discharges. However, figure 19(e) shows that except for the start-up MHD activity around 0.25 s, these discharges are free of rotating  $n = 1$  MHD. Contributing factors to the observed stability are the lack of ELMs and EPMS in these lithium-conditioned discharges. However, further research is required to demonstrate in detail which equilibrium properties render these types of discharges immune to the ‘triggerless onset’  $n = 1$  modes.

## 9. Disruptions with the largest stored energy

It was noted in section 3 that the largest stored-energy disruptions typically occur during the plasma current ramp-down. This section describes the phenomenology of those disruptions in more detail.

An example of large stored-energy disruption during the ramp-down is shown in figure 20. As shown in figure 20(a), this is a 1.1 MA discharge heated by 4 MW of neutral beams. This discharge is operating stably until the solenoid reaches



**Figure 19.** Time evolution of (a) the plasma current, (b) the normalized  $\beta$ , (c)  $q^*$ , (d) the minimum safety factor, and (e) the low-frequency rotating  $n = 1$  MHD detector. The two discharges selected are among the longest ever achieved in NSTX.

its  $I_{OH} = -24$  kA current limit at  $t = 862$  ms. At this time, indicated by a vertical dashed line in the figure, the solenoid current is ramped back to zero by the power supply control software, applying a very large negative loop voltage to the plasma (see figure 20(b)). The plasma current then begins to decrease, while the internal inductance  $l_i$  increases. This change to the current profile results in the inner plasma-wall gap decreasing to zero (the lack of PF coils on the high-field side of the ST often results in the inner plasma-wall gap being poorly controlled). The disruption occurs at  $t = 870.3$  ms. Figure 20(c) indicates that the stored energy at the time of disruption was  $\sim 300$  kJ, with minimal decrease during the short (8 ms) pre-disruption plasma current ramp-down phase.

In order to understand the time-scales and dynamics for this disruptions, we examine the neutron and ultra-soft x-ray (USXR) emission; these are shown separately in figures 20(d) and (e) respectively, and for a time window localized to the thermal quench in figure 20(f). The neutron emission is dominated by beam-target reactions, and so is a good proxy for the fast particle content. We see that this emission drops in two steps. The USXR emission is measured with a pin-hole camera through 100 mm beryllium filters [186]; these filters are the thickest available in the NSTX arrays and generally result in the detected x-rays originating from within the H-mode pedestal top. The two separate phases of the thermal quench are readily discernible in the USXR emission. The first rapid energy loss phase has a duration of roughly 40–60  $\mu$ s, and appears to correspond to the very rapid loss of the H-mode pedestal once the plasma becomes inner-wall limited. The second energy loss phase has a duration of  $\sim 200$   $\mu$ s, corresponding to the loss of core confinement. These two phases are separated by a duration of 1500  $\mu$ s. Note that the typical Alfvén times

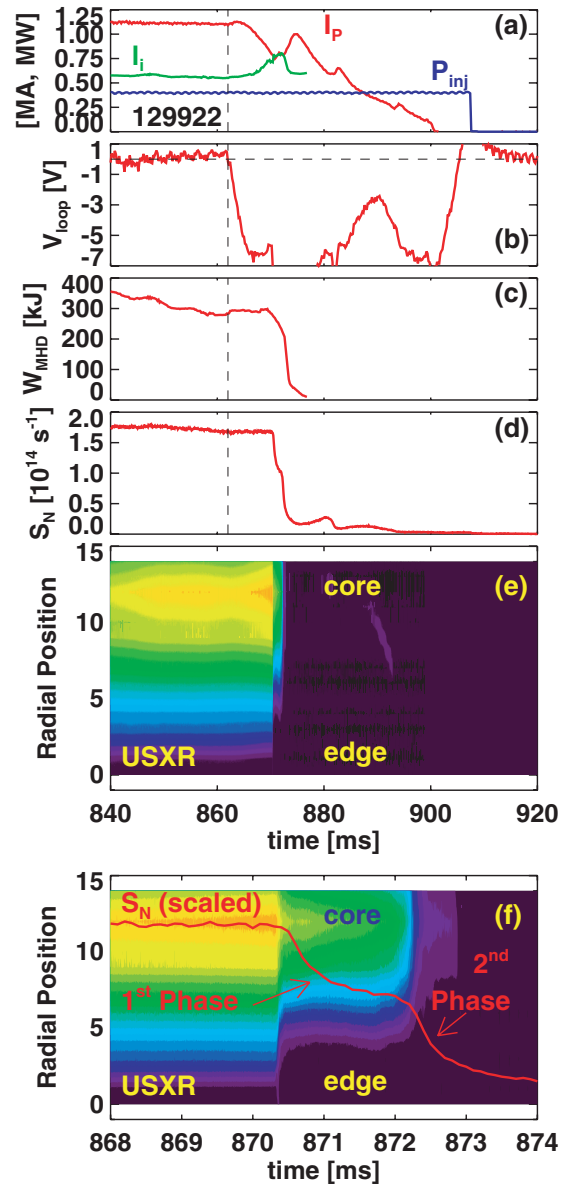


**Figure 20.** Time evolution of various quantities during the thermal quench of a large stored-energy disruption. Shown are the (a) the plasma current, internal inductance, and heating power, (b) the loop voltage, (c) the stored energy, (d) the neutron emission ( $S_N$ ), (e) contours of soft x-ray emission, and (f) the same soft x-ray emission isolating a narrow window during the thermal quench. Also shown in frame (f) is a scaled version of the neutron emission, as well as labels of the two phases of the thermal quench.

$\tau_A = 2\pi R_0/V_A$  are 2–8  $\mu$ s, and it is clear that at least the first of these collapses occurs on a near-Alfvénic time-scale.

This type of disruption, initiated by loop-voltage reversal, is responsible for 21 of the 22 largest stored-energy disruptions, and all but one of the disruptions with stored energy greater than 275 kJ, in NSTX during the time under consideration. We note that while this disruption was caused by incorrect initiation of the plasma current ramp-down, it clearly shows that such large  $W_{MHD}$  disruptions are possible, for instance, in the case of failure of a current drive actuator, and accounting for them should be part of the design of next-step STs. We also note that the discharges with the very highest stored energy,



such as the 460 kJ case noted in section 3, have substantial stored-energy loss before the disruption; see figure 3 of [103] for this example.

## 10. Summary and implications for next-step devices

This paper has documented the following significant points with regard to disruptivity in high- $\beta$  NSTX plasmas.

- The disruption rate in NSTX is rather high, with only about 25% of discharges reaching a ramp-down phase (section 3).
- There is often a significant loss of plasma current and stored energy in the phase following an MHD mode but preceding the disruptions (section 3).
- The disruptivity of NSTX plasmas is independent of, or even decreases with, the normalized- $\beta$  (sections 4 and 5).
- The disruptivity increases rapidly for  $q^* < 2.7$ . This is well above the ideal MHD low- $q$  limit, and is instead related to various operational issues that occur at higher current (sections 4 and 7).
- Strong shaping and broad current and pressure profiles are critical in reducing the disruptivity (section 4).
- The disruptivity increases considerably when the core rotation drops beneath  $\sim 8$  kHz, corresponding to  $F_{T,\text{core}}/F_A < 0.04$  (section 4).
- Use of  $n = 1$  dynamic error field correction and RWM control results in a significant decrease in the disruptivity (section 5).
- While there appear to be certain regions of forbidden operation (low  $q^*$  for instance), it is generally not possible to point to any single parameter as being responsible for minimizing disruptivity. Rather, the combination of boundary shaping, strong rotation, and optimal thermal and current profiles is critical. Achieving these conditions requires proper formation of the discharge, and control techniques for maintaining these conditions must be developed.
- There are a class of early flat-top disruptions due to MHD modes that develop at rational surfaces where they enter the plasma. The disruption results when these modes brake the plasma rotation sufficiently that the plasma rotation is stopped. The key to avoiding these disruptions has not been to avoid the MHD modes altogether. Rather, it is important to arrange the early discharge evolution so that the rotation damping is less severe (section 6).
- In otherwise quiescent discharges, core  $n = 1$  modes often grow when  $q_{\text{min}}$  drops below 1.25. When disturbances such as ELMs or EPMs are present, these  $n = 1$  modes can be triggered at  $q_{\text{min}}$  as high as 1.5 (section 8).
- The largest stored-energy disruptions occur when the loop voltage is reversed at full current and heating power. These show a two-part thermal quench, with the time-scales of a few tens of Alfvén times (section 9).

With regard to next-step spherical torus devices, the implications are rather obvious. The equilibria likely should be strongly shaped, consistent with robust vertical stability and boundary control. The current drive actuators should be arranged to provide a broad current profile. This is of course the natural result in the case of the bootstrap current.

However, many next-step ST designs rely on neutral beam current drive, and those neutral beams should be configured to elevate  $q_{\text{min}}$  sufficiently above one that these core  $n = 1$  modes can be avoided. Furthermore, it appears that internal transport barrier scenarios may be less desirable, due to the increased disruptivity as the pressure peaking is increased. Transients that could destabilize MHD modes or result in the loss of boundary control should be avoided. Robust current ramp-down and soft landing strategies should be developed.

Much of the research required to meet these requirements will be carried out in the 2 MA class upgrades to existing STs. These are, in the United States, NSTX-Upgrade [139, 187], and in the UK, MAST-Upgrade [188]. Both devices will have great flexibility to control the central safety factor by varying the density, current, and neutral beam selection, allowing the optimal value of  $q_{\text{min}}$  to be better determined. The upgraded magnet capabilities will allow disruption avoidance studies in the  $I_p$  flat-top for 20–30 current relaxation times [139] in NSTX-Upgrade. This will provide an important test of error field reduction, RWM avoidance, current profile maintenance and boundary control, all with the goal of eliminating flat-top disruptions. However, it is clear that better control of both the current ramp-up and early flat-top, and the discharge termination phase, will be required to fully exploit the capabilities of that upgrade. With regard to the ramp-up, the significantly larger solenoid current and heating capability in NSTX-U may allow the plasma current to be ramped up more slowly than is shown in figures 14 and 15. This may in turn provide an additional degree of freedom in understanding and avoiding those deleterious modes that occur during the current ramp-up.

## Acknowledgments

We would also like to thank R. Maingi and A. Bortolon for helpful discussion. This research was funded by the United States Department of Energy under contract DE-AC02-09CH11466.

## Appendix. Determining the time of the first $I_p$ deviation

As described in sections 2 and 4, the disruptivity statistics are defined against the time of first  $I_p$  deviation. This is the time when a drop in  $I_p$  is flagged as being indicative of the beginning of the disruption process. To compute this time, the following procedure is defined.

First, the fractional deviation of the plasma current from the requested value is computed as  $\text{test} = (I_{p,\text{req}} - I_p)/I_{p,\text{req}}$ . This quantity is compared with a threshold value, given by the following rule:  $\text{threshold} = 0.03$  for  $t > t_{\text{SoFT}} + 75$  ms,  $\text{threshold} = 0.04$  for  $t_{\text{SoFT}} + 20$  ms  $< t < t_{\text{SoFT}} + 75$  ms, and  $\text{threshold} = 0.08$  for  $t < t_{\text{SoFT}} + 20$  ms ( $t_{\text{SoFT}}$  is the time of the start of the  $I_p$  flat-top). Allowing larger values of the threshold earlier in the discharge allows for the occasional non-disruptive  $I_p$  deviations at the beginning of the discharge to not register in the algorithm.

A reduced set of samples that are within 180 ms of the current quench ( $t_{\text{quench}}$ ) and that satisfy  $\text{test} > \text{threshold}$  are chosen for further examination. The time window of 180 ms

is chosen to be short enough to eliminate most plasma current deviations that are not associated with disruptions, while being long enough to find the time of disruption initiation for cases where the disruption process is drawn out for a long duration. The first time in that reduced set that satisfies  $V_{\text{loop}} > 3.5$  V, a value that is anomalously high for the flat-top of any beam heated discharge, is defined as  $t_{I_p, \text{Dev}}$ . If no time is found with  $V_{\text{loop}} > 3.5$  V, then the  $t_{I_p, \text{Dev}}$  is found at the earliest time in the set of samples that satisfies  $\int_{t_{I_p, \text{Dev}}}^{t_{I_p, \text{Dev}}+30 \text{ms}} V_{\text{loop}} dt > 2.0 \text{ V} \cdot 30 \text{ms}$ , i.e. the first time when the subsequent average of the loop voltage over a 30 ms period exceeds 2.0 V. If no time is found meeting this criterion, then  $t_{I_p, \text{Dev}}$  is set equal to  $t_{\text{quench}}$ . Note that there are rare cases where the relevant time of first  $I_p$  deviation may be earlier than 180 ms. Even more rare are cases where the plasma may, with the 180 ms window, fully recover from the events leading to the registered  $I_p$  deviation, then have a new MHD event that initiates a new disruption process.

## References

- [1] ITER Physics Basis Editors *et al* 1999 *Nucl. Fusion* **39** 2137
- [2] Riccardo V. *et al* 2002 *Plasma Phys. Control Fusion* **44** 905
- [3] Riccardo V., Loarte A. and JET EFDA Contributors 2005 *Nucl. Fusion* **45** 1427
- [4] Federici G. 2006 *Phys. Scr.* **T124** 1
- [5] Loarte A. *et al* 2007 *Phys. Scr.* **T128** 222
- [6] Hender T.C. *et al* Progress in the ITER Physics Basis: chapter 3. MHD stability, operational limits and disruptions 2007 *Nucl. Fusion* **47** S128–202
- [7] Arnoux G. *et al* 2008 *Nucl. Fusion* **49** 085038
- [8] Riccardo V. *et al* 2010 *Plasma Phys. Control. Fusion* **52** 024018
- [9] Humphreys D.A. and Whyte D.G. 2000 *Phys. Plasmas* **7** 4057
- [10] Riccardo V., Barabaschi P. and Sugihara M. 2005 *Plasma Phys. Control. Fusion* **47** 117
- [11] Wesley J.C. *et al* 2006 *Proc. 21st Int. Conf. on Fusion Energy 2006 (Chengdu, China, 2006)* (Vienna: IAEA) CD-ROM file IT/P1-21 and <http://www-naweb.iaea.org/naweb/naweb.nsf/0/55978189100000000000000000000000>
- [12] Gerhardt S.P., Menard J.E. and the NSTX Team 2009 *Nucl. Fusion* **49** 025005
- [13] Wesley J.C. *et al* 2010 *Proc. 23rd Int. Conf. on Fusion Energy 2010 (Daejeon, Korea, 2010)* (Vienna: IAEA) CD-ROM file ITR/P1-26 and <http://www-naweb.iaea.org/naweb/naweb.nsf/0/55978189100000000000000000000000>
- [14] Shibata Y. *et al* 2010 *Nucl. Fusion* **50** 025012
- [15] Sugihara M. *et al* 2007 *Nucl. Fusion* **47** 337
- [16] Rosenbluth M.N. and Putvinski S.V. 1997 *Nucl. Fusion* **37** 1355
- [17] Yoshino R., Tokuda S. and Kawano Y. 1999 *Nucl. Fusion* **39** 151
- [18] Yoshino R. and Tokuda S. 2000 *Nucl. Fusion* **40** 1293
- [19] Gill R.D. *et al* 2002 *Nucl. Fusion* **42** 1039
- [20] Tamai H. *et al* 2002 *Nucl. Fusion* **42** 290
- [21] Forster M. *et al* 2011 *Nucl. Fusion* **51** 043003
- [22] Sizyuk V. and Hassanein A. 2009 *Nucl. Fusion* **49** 095003
- [23] Lazarus E.A. *et al* 1991 *Phys. Fluids* **3** 2220
- [24] Hofmann F., Dutch M.J., Ward D.J., Anton M., Furno I., Lister J.B. and Moret J.-M. 1997 *Nucl. Fusion* **37** 681
- [25] Hofmann F., Favre A., Isoz P.-F., Martin Y., Moret J.-M. and Nieswand C. 2000 *Nucl. Fusion* **40** 767
- [26] Kessel C.E., Heitzenroeder P. and Jun C. 2001 *Nucl. Fusion* **41** 953
- [27] Humphreys D.A. *et al* 2009 *Nucl. Fusion* **49** 115003
- [28] Strait E.J., Lao L.L., Luxon J.L. and Reis E.E. 1991 *Nucl. Fusion* **31** 527
- [29] Granetz R.S. *et al* 1996 *Nucl. Fusion* **36** 545
- [30] Neyatani Y., Yoshino R., Nakamura Y. and Sakurai S. 1999 *Nucl. Fusion* **39** 559
- [31] Counsell G.F. *et al* 2007 *Plasma Phys. Control. Fusion* **49** 435
- [32] Riccardo V. *et al* 2009 *Nucl. Fusion* **49** 055012
- [33] Pautasso G. *et al* 2011 *Nucl. Fusion* **51** 043010
- [34] Gerhardt S.P. *et al* 2012 *Nucl. Fusion* **52** 063005
- [35] De Vries P.C. *et al* 2011 *Nucl. Fusion* **51** 053018
- [36] Troyon F. *et al* 1984 *Plasma Phys. Control. Fusion* **26** 209
- [37] Menard J.E. *et al* 1997 *Nucl. Fusion* **37** 595
- [38] Miller R.L. *et al* 1997 *Phys. Plasmas* **4** 1062
- [39] Strait E.J. 1994 *Phys. Plasmas* **1** 1415
- [40] Turnbull A. *et al* 1999 *Phys. Plasmas* **6** 1113
- [41] Howl W. *et al* 1992 *Phys. Fluids B* **4** 1724
- [42] Bondeson A. and Ward D.J. 1994 *Phys. Rev. Lett.* **72** 2709
- [43] Ward D.J. and Bondeson A. 1995 *Phys. Plasmas* **2** 1570
- [44] Strait E.J. *et al* 1999 *Nucl. Fusion* **39** 1977
- [45] Garofalo A.M. *et al* 1999 *Phys. Plasmas* **6** 1893
- [46] Sabbagh S.A. *et al* 2002 *Phys. Plasmas* **9** 2085
- [47] Sabbagh S.A. *et al* 2004 *Nucl. Fusion* **44** 560
- [48] Sontag A.C. *et al* 2005 *Phys. Plasmas* **12** 056112
- [49] Sabbagh S.A. *et al* 2006 *Nucl. Fusion* **46** 635
- [50] Sontag A.C. *et al* 2007 *Nucl. Fusion* **47** 1005
- [51] Strait E.J. *et al* 2004 *Phys. Plasmas* **11** 2505
- [52] Sabbagh S.A. *et al* 2006 *Phys. Rev. Lett.* **97** 045004
- [53] Menard J.E. *et al* 2004 *Phys. Plasmas* **11** 639
- [54] Wesson J.A. *et al* 1989 *Nucl. Fusion* **29** 641
- [55] Kaye S.M. *et al* 1988 *Nucl. Fusion* **28** 1963
- [56] de Vries P.C., Johnson M.F., Segui I. and JET EFDA Contributors 2009 *Nucl. Fusion* **49** 055011
- [57] Shimada M. *et al* 2007 Progress in the ITER Physics Basis: chapter 1. Overview and summary *Nucl. Fusion* **47** S1
- [58] Murakami M. *et al* 1976 *Nucl. Fusion* **16** 347
- [59] Greenwald M. *et al* 1988 *Nucl. Fusion* **28** 2199
- [60] Maingi R. *et al* 1997 *Phys. Plasmas* **4** 1752
- [61] Greenwald M. *et al* 2002 *Plasma Phys. Control. Fusion* **44** R27
- [62] Gates D.A. *et al* 2012 *Phys. Rev. Lett.* **108** 165001
- [63] Wagner F. *et al* 1982 *Phys. Rev. Lett.* **49** 1408
- [64] Rebut P.H. *et al* 1985 *Proc. 10th Int. Conf. on Plasma Physics and Controlled Nuclear Fusion Research 1984 (London, 1984)* vol 2 (Vienna: IAEA) p 197
- [65] Suttrop W. *et al* 1997 *Nucl. Fusion* **37** 119
- [66] Salzedas F. *et al* 2002 *Phys. Rev. Lett.* **88** 075002
- [67] Chang Z. *et al* 1995 *Phys. Rev. Lett.* **74** 4663
- [68] La Haye R.J. *et al* 1997 *Nucl. Fusion* **37** 397
- [69] Zohm H. *et al* 1997 *Plasma Phys. Control. Fusion* **39** B237
- [70] Sauter O. *et al* 1997 *Phys. Plasmas* **4** 1654
- [71] Gates D.A. *et al* 1997 *Nucl. Fusion* **37** 1593
- [72] La Haye R.J. *et al* 2006 *Phys. Plasmas* **13** 055501
- [73] Gerhardt S.P. *et al* 2009 *Nucl. Fusion* **49** 032003
- [74] La Haye R.J. *et al* 2012 *Phys. Plasmas* **19** 062506
- [75] BATTERY R. *et al* 2002 *Phys. Rev. Lett.* **88** 125005
- [76] Gibson K.J. *et al* 2010 *Plasma Phys. Control. Fusion* **52** 124041
- [77] Garofalo A.M., LaHaye R.J. and Scoville J.T. 2002 *Nucl. Fusion* **42** 1335
- [78] Menard J.E. *et al* 2010 *Nucl. Fusion* **50** 045008
- [79] Okabayashi M. *et al* 2005 *Nucl. Fusion* **45** 1715
- [80] Garofalo A.M. *et al* 2007 *Nucl. Fusion* **47** 1121
- [81] Okabayashi M. *et al* 2009 *Nucl. Fusion* **49** 125003
- [82] Gantenbein G. *et al* 2000 *Phys. Rev. Lett.* **85** 1242
- [83] Isayama A. *et al* 2000 *Plasma Phys. Control. Fusion* **42** L37
- [84] Petty C.C. *et al* 2004 *Nucl. Fusion* **44** 243
- [85] Maraschek M. *et al* 2005 *Nucl. Fusion* **45** 1369
- [86] Humphreys D.A. *et al* 2006 *Phys. Plasmas* **13** 056113
- [87] La Haye R.J. *et al* 2005 *Nucl. Fusion* **45** L37
- [88] Abdou M. 1995 *Fusion Eng. Des.* **27** 111
- [89] Peng Y.-K.M. *et al* 2005 *Plasma Phys. Control. Fusion* **47** B263
- [90] Wilson H.R. *et al* 2004 *Proc. 20th Int. Conf. on Fusion Energy 2004 (Vilamoura, Portugal, 2004)* (Vienna: IAEA)

- CD-ROM file FT/3-1Ra and <http://www-naweb.iaea.org/napc/physics/fec/fec2004/datasets/index.html>
- [91] Voss G.M. *et al* 2008 *Fusion Eng. Des.* **83** 1648
- [92] Peng Y.-K.M. *et al* 2008 *Proc. 22nd Int. Conf. on Fusion Energy 2008 (Geneva, Switzerland, 2008)* (Vienna: IAEA) CD-ROM file FT/P3-14 and <http://www-naweb.iaea.org/napc/physics/FEC/FEC2008/html/index.htm>
- [93] Peng Y.-K.M. *et al* 2009 *Fusion Sci. Technol.* **56** 957
- [94] Peng Y.-K.M. *et al* 2010 *Proc. 23rd Int. Conf. on Fusion Energy 2010 (Daejeon, Korea, 2010)* (Vienna: IAEA) CD-ROM file FT/P2-Ra and <http://www-naweb.iaea.org/napc/physics/FEC/FEC2010/html/index.htm>
- [95] Stambaugh R.D. *et al* 2010 *Candidates for a Fusion Nuclear Science Facility (FDF and ST-CTF) 37th EPS Conf. on Plasma Physics (Dublin, Ireland, 2010)* paper P2.110 <http://ocs.ciemat.es/EPS2010PAP/pdf/P2.110.pdf>
- [96] Ono M. *et al* 2000 *Nucl. Fusion* **40** 557
- [97] Stevenson T. *et al* 2002 A neutral beam injector upgrade for NSTX *PPPL Report* 3651
- [98] Gerhardt S.P. *et al* 2012 *Fusion Sci. Technol.* **61** 11
- [99] Wilson J.R. *et al* 2003 *Phys. Plasmas* **10** 1733
- [100] Lao L.L. 1985 *Nucl. Fusion* **25** 1611
- [101] Sabbagh S.A. *et al* 2001 *Nucl. Fusion* **41** 1601
- [102] LeBlanc B.P. *et al* 2003 *Rev. Sci. Instrum.* **74** 1659
- [103] Gerhardt S.P. *et al* 2011 *Nucl. Fusion* **51** 073031
- [104] Bell R.E. and Feder R. 2010 *Rev. Sci. Instrum.* **81** 10D724
- [105] La Haye R.J. *et al* 2002 *Phys. Plasmas* **9** 2051
- [106] Zhu W. *et al* 2006 *Phys. Rev. Lett.* **96** 225002
- [107] Garofalo A.M. 2008 *Phys. Rev. Lett.* **101** 195005
- [108] Park J.-K., Boozer A.H. and Menard J.E. 2009 *Phys. Rev. Lett.* **102** 065002
- [109] Sabbagh S.A. *et al* 2010 *Nucl. Fusion* **50** 025020
- [110] Cole A.J. *et al* 2011 *Phys. Rev. Lett.* **106** 225002
- [111] Sabbagh S.A. *et al* 2010 *Proc. 23rd Int. Conf. on Fusion Energy 2010 (Daejeon, Korea, 2010)* (Vienna: IAEA) CD-ROM file EXS/5-5 and <http://www-naweb.iaea.org/napc/physics/FEC/FEC2010/html/index.htm>
- [112] Gerhardt S.P. *et al* 2010 *Plasma Phys. Control. Fusion* **52** 104003
- [113] Gerhardt S.P. *et al* 2010 *Nucl. Fusion* **50** 064015
- [114] Canik J.M. *et al* 2010 *Phys. Rev. Lett.* **104** 045001
- [115] Canik J.M. *et al* 2010 *Nucl. Fusion* **50** 034012
- [116] Canik J.M. *et al* 2010 *Nucl. Fusion* **50** 064016
- [117] Ferron J.R. *et al* 1998 *Nucl. Fusion* **38** 1055
- [118] Gates D.A. *et al* 2006 *Nucl. Fusion* **46** 17
- [119] Kolemen E. *et al* 2010 *Nucl. Fusion* **50** 105010
- [120] Kolemen E. *et al* 2011 *Nucl. Fusion* **51** 113024
- [121] Kugel H. *et al* 2008 *Phys. Plasmas* **15** 056118
- [122] Bell M.G. *et al* 2009 *Plasma Phys. Control. Fusion* **51** 124054
- [123] Menard J.E. *et al* 2005 *Nucl. Fusion* **45** 539
- [124] Menard J.E. *et al* 2006 *Phys. Rev. Lett.* **97** 095002
- [125] Gerhardt S.P. *et al* 2011 *Nucl. Fusion* **51** 033004
- [126] Kugel H.W. *et al* 2009 *Fusion Eng. Des.* **84** 1125
- [127] Raman R. *et al* 2006 *Phys. Rev. Lett.* **97** 175002
- [128] Raman R. *et al* 2007 *Nucl. Fusion* **47** 792
- [129] Raman R. *et al* 2009 *Nucl. Fusion* **49** 065006
- [130] Raman R. *et al* 2010 *Phys. Rev. Lett.* **104** 095003
- [131] Nelson B.A. *et al* 2011 *Nucl. Fusion* **51** 063008
- [132] Yushmanov P.N. *et al* 1990 *Nucl. Fusion* **30** 1999
- [133] Lazarus E.A. *et al* 1992 *Phys. Fluids B* **4** 3644
- [134] Lazarus E. *et al* 1996 *Phys. Rev. Lett.* **77** 2714
- [135] Sabbagh S.A. *et al* 1996 *Proc. 16th Int. Conf. on Fusion Energy (Montreal, Canada, 7–11 October 1996)* (Vienna: IAEA) AP2-17
- [136] Sips A.C.C. *et al* 2005 *Plasma Phys. Control. Fusion* **47** A19
- [137] Ferron J.R. *et al* 2005 *Phys. Plasmas* **12** 056126
- [138] Menard J.E. *et al* 2003 *Nucl. Fusion* **43** 330
- [139] Gerhardt S.P. *et al* 2012 *Nucl. Fusion* **52** 083020
- [140] Reimerdes H. *et al* 2005 *Nucl. Fusion* **45** 368
- [141] Reimerdes H. *et al* 2007 *Nucl. Fusion* **49** B349
- [142] Mansfield D.K. *et al* 2009 *J. Nucl. Mater.* **390–391** 764
- [143] Maingi R. *et al* 2009 *Phys. Rev. Lett.* **103** 075001
- [144] Boyle D.P. *et al* 2011 *Plasma Phys. Control. Fusion* **53** 105011
- [145] Scotti F. *et al* 2011 *J. Nucl. Mater.* **415** S405
- [146] Boozer A.H. 2001 *Phys. Rev. Lett.* **86** 5059
- [147] Reimerdes H. *et al* 2004 *Phys. Rev. Lett.* **93** 135002
- [148] Liu Y. *et al* 2008 *Phys. Plasmas* **15** 112503
- [149] Berkery J.W. *et al* 2010 *Phys. Rev. Lett.* **104** 035003
- [150] Berkery J.W. *et al* 2010 *Phys. Plasmas* **17** 082504
- [151] Berkery J.W. *et al* 2011 *Phys. Rev. Lett.* **106** 075004
- [152] Berkery J.W. *et al* 2011 *Phys. Plasmas* **18** 072501
- [153] Reimerdes H. *et al* 2011 *Phys. Rev. Lett.* **106** 215002
- [154] Berkery J.W. *et al* 2012 Global mode control and stabilization for disruption avoidance in high- $\beta$  ST plasmas (IAEA FEC, San Diego, CA) paper EX/P8-07
- [155] Bortolon A. 2012 Interplay between coexisting MHD instabilities mediated by energetic ions in NSTX H-mode plasmas *APS-DPP Meeting (Providence, RI)* BAPS.2012.DPP.JI2.2 and <http://meetings.aps.org/link/BAPS.2012.DPP.JI2.2>
- [156] Heidbrink W.W. *et al* 2003 *Nucl. Fusion* **43** 883
- [157] Pankin A. *et al* 2004 *Comput. Phys. Commun.* **159** 157
- [158] Hawryluk R.J. *et al* 1980 An empirical approach to tokamak transport *Physics of Plasmas Close to Thermonuclear Conditions* ed B. Coppi *et al* (Brussels: CEC, 1980) vol 1, pp 19–46
- [159] Soukhanovskii V.A. *et al* 2004 *Rev. Sci. Instrum.* **75** 4320
- [160] Maingi R. *et al* 2004 *Plasma Phys. Control. Fusion* **46** A305
- [161] Gates D.A. *et al* 2003 *Phys. Plasmas* **10** 1659
- [162] Gates D.A. *et al* 2007 *Nucl. Fusion* **47** 1376
- [163] Gates D.A. *et al* 2009 *Nucl. Fusion* **49** 104016
- [164] Bush C. *et al* 2003 *Phys. Plasmas* **10** 1755
- [165] Maingi R. *et al* 2010 *Nucl. Fusion* **50** 064010
- [166] Kaye S.M. *et al* 2011 *Nucl. Fusion* **51** 113019
- [167] Martin Y.R. *et al* 2008 *J. Phys.: Conf. Ser.* **123** 012033
- [168] Maingi R. *et al* 2010 *Phys. Rev. Lett.* **105** 135004
- [169] Maingi R. *et al* 2009 *J. Nucl. Mater.* **390–391** 440
- [170] Fredrickson E.D., Chen L. and White R. 2003 *Nucl. Fusion* **43** 1258
- [171] Maingi R. *et al* 2005 *Nucl. Fusion* **45** 1066
- [172] Grimm R.C., Greene J.M. and Johnson J.L. 1976 Computation of the magnetohydrodynamic spectrum in axisymmetric toroidal confinement systems *Methods in Computational Physics* vol 16, ed J. Killeen (New York: Academic) pp 253–80
- [173] Park W. *et al* 1999 *Phys. Plasmas* **6** 1796–803
- [174] Breslau J. *et al* 2011 *Nucl. Fusion* **51** 063027
- [175] Levinton F. and Yuh H. 2008 *Rev. Sci. Instrum.* **79** 10F522
- [176] Turco F. *et al* 2010 *Nucl. Fusion* **50** 095010
- [177] Brennan D.P., Turnbull A.D., Chu M.S., La Haye R.J., Lao L.L., Osborne T.H. and Galkin S.A. 2007 *Phys. Plasmas* **14** 056108
- [178] Chapman I.T. *et al* 2010 *Nucl. Fusion* **50** 045007
- [179] Chapman I.T. *et al* 2011 *Nucl. Fusion* **51** 073040
- [180] Brennan D.P., Kim C.C. and La Haye R.J. 2012 *Nucl. Fusion* **52** 033004
- [181] Gude A. *et al* 1999 *Nucl. Fusion* **39** 127
- [182] Okabayashi M. *et al* 2011 *Phys. Plasmas* **18** 056112
- [183] Buttery R. *et al* 2008 *Phys. Plasmas* **15** 056115
- [184] Hender T.C. *et al* 2004 *Nucl. Fusion* **44** 788
- [185] Buratti P. *et al* 2012 *Nucl. Fusion* **52** 1
- [186] Stutman D. *et al* 1999 *Rev. Sci. Instrum.* **70** 572
- [187] Menard J.E. *et al* 2012 *Nucl. Fusion* **52** 083015
- [188] Stork D. *et al* 2010 *Proc. 23rd Int. Conf. on Fusion Energy 2010 (Daejeon, Korea, 2010)* (Vienna: IAEA) CD-ROM file ICC/P5-06 and <http://www-naweb.iaea.org/napc/physics/FEC/FEC2010/html/index.htm>